

Spectral and Timing Analysis of Transient X-ray Pulsars

*A thesis submitted to the
Physics Department of the University of Crete
for the award of the degree*

of

Master of Science

by

Konstantinos Droudakis

Under the guidance of

Prof. Andreas Zezas



**Department of Physics
University of Crete**

Heraklion, Greece

October 2022

Acknowledgments

I would like to express my profound gratitude to Prof. Andreas Zezas for his guidance and advice on this project and on my M.Sc. studies. His exceptional knowledge and experience in the field of Astrophysics assisted me greatly throughout my journey. I would also like to acknowledge Dr. Pablo Reig for teaching me the operation of the XRONOS software and helping with finding the pulsar's period. Finally, I would like to thank my family and friends for their support during the good, as well as the difficult times.

Abstract

We present the pulse profiles and the spectral and timing analysis of the Be/X-ray binary pulsar SXP 4.78 using data obtained from the combined observations of NuSTAR and Swift during its outburst in mid-November 2018. With the application of appropriate theoretical models, we extract information regarding the physical and geometrical parameters of the accretion column, as well as the accretion disk. In addition, we calculate an upper boundary for the magnetic field strength of the neutron star, $B \lesssim 22.7 \cdot 10^{12} \text{ G}$. We also find evidence of an evolved accretion disk, reaching close to the surface of the pulsar. Finally, we study the changes of the accretion column parameters in respect to time. The results are discussed and compared with previous studies.

Abstract in Greek

Παρουσιάζουμε το παλμικό προφίλ και τη φασματική και χρονική ανάλυση του πάλσαρ SXP 4.78, μέρος ενός διπλού συστήματος Be/ακτίνων-Χ. Η ανάλυση έγινε με τη χρήση δεδομένων από ταυτόχρονες παρατηρήσεις των διαστημικών παρατηρητήριων NuSTAR και Swift κατά τη διάρκεια έκλαμψής του στα μέσα Νοεμβρίου του 2018. Με εφαρμογή κατάλληλων θεωρητικών μοντέλων εξάγουμε πληροφορίες όσον αφορά τις φυσικές και γεωμετρικές παραμέτρους της κολώνας προσαύξησης, καθώς και του δίσκου προσαύξησης. Επιπλέον, υπολογίσαμε ένα άνω όριο για την ένταση του μαγνητικού πεδίου του αστερά νετρονίων, $B \lesssim 22.7 \cdot 10^{12} G$. Επίσης, εντοπίσαμε ενδείξεις ενός εξελιγμένου δίσκου προσαύξησης, ο οποίος φτάνει την επιφάνεια του πάλσαρ. Τέλος, μελετήθηκε και η αλλαγή των παραμέτρων της κολώνας προσαύξησης συναρτήσει του χρόνου. Τα αποτελέσματα συγκρίνονται και με προηγούμενες μελέτες.

Table of Contents

Acknowledgments	i
Abstract	iii
Abstract in Greek	v
Table of Contents	ix
List of Figures	xi
List of Tables	xiii
Chapter 1	Introduction
	1
1.1	Pulsars 1
1.2	X-ray Binaries 1
1.2.1	High Mass X-ray Binaries 2
1.2.2	Be/X-ray Binaries 2
1.3	Transient X-ray Pulsars 2
1.4	Accretion 3
1.4.1	Accretion in Binary Systems 4
1.4.2	Accretion Disk 5
1.4.3	Accretion Column 6
1.5	Pulse Profile 8
1.6	Cyclotron Resonant Scattering Features 9
1.7	Purpose of this Project 10

Chapter 2	Observations and Methodology	13
2.1	The Target	13
2.2	Observational Instruments	13
2.2.1	The NuSTAR Observatory	14
2.2.2	The Neil Gehrels Swift Observatory	14
2.3	Observations	15
2.4	Methodology	16
2.4.1	Data Reduction	17
	NuSTAR Data Reduction	17
	Swift Data Reduction	18
	Pile-up check for the Swift Observation 3	21
2.4.2	Spectral Analysis	22
	Compmag	23
	Gauss	24
	Diskbb	25
	Gabs	25
2.4.3	Timing Analysis	25
	Pulse Period Search	26
	Phase Binning	27
Chapter 3	Results	31
3.1	Phase Averaged Analysis	31
3.1.1	Initial Models	31
3.1.2	Model A Fitting	34
3.1.3	Model B Fitting	38
3.2	Pulse Profile of SXP 4.78	38
3.3	Phase Resolved Analysis	41
3.3.1	Observation 1	42
3.3.2	Observation 2	43
3.3.3	Observation 3	44
3.3.4	Cyclotron Line Search	45

Chapter 4	Discussion	47
4.1	Phase Averaged Analysis	47
4.1.1	Accretion Disk	47
4.1.2	Magnetic Field Strength	48
4.2	Pulse Profiles	49
4.3	Phase Resolved Analysis	49
4.4	Time Evolution	50
4.5	Further Work	50
Chapter 5	Conclusion	53
References		55
Declaration		59

List of Figures

1.1	Schematic of a Be/X-ray binary system	3
1.2	Stellar wind accretion schematic	4
1.3	Illustration of Roche lobe accretion	5
1.4	Schematic of an accretion disk and accretion column	6
1.5	Schematic of an accretion column from Becker and Wolff, 2007	7
1.6	Theoretical column-integrated count rate spectrum of Her X-1 from Becker and Wolff, 2007	8
1.7	Schematic of pencil beam and fan beam	9
1.8	Pulse profile of the Crab pulsar	10
2.1	Optical image of the location of SXP 4.78	14
2.2	Depiction of the NuSTAR space observatory	15
2.3	Depiction of the Neil Gehrels Swift space observatory	16
2.4	Count-rate as a function of time during the 3 observational instances	17
2.5	Region file selection for the source and background	18
2.6	Sky image of SXP 4.78 from Swift observation 00088816001 using the PC mode	19
2.7	Sky image of SXP 4.78 from Swift observation 00010977004 using the WT mode	20
2.8	Pile-up modeling of Swift PC mode observation 00088816001	21
2.9	Initial spectrum of SXP 4.78 from every observational instance . . .	22
2.10	Final spectrum of SXP 4.78 from every observational instance . . .	23
2.11	Power spectrum of the lightcurve of NuSTAR FPMA observation 30361003002	26

2.12	Chi-squared - period offset diagram of the lightcurve NuSTAR FPMA observation 30361003002	27
2.13	The pulse profile of Obs1 NuSTAR FPMA	29
3.1	Energy spectrum of Observation 1, Model O1 fit, residuals and ratio	32
3.2	Energy spectrum of Observation 1, Model O2 fit, residuals and ratio	33
3.3	Energy spectrum of Observation 1, Model A fit, residuals and ratio	35
3.4	Energy spectrum of Observation 2, Model A fit, residuals and ratio	36
3.5	Energy spectrum of Observation 3, Model A fit, residuals and ratio	37
3.6	Pulse profile of Observation 3	38
3.7	Pulse profile of Observation 2	39
3.8	Pulse profile of Observation 1	40
3.9	Phase resolved analysis results of the 4 variable parameters of Model A for Obs1.	42
3.10	Phase resolved analysis results of the 4 variable parameters of Model A for Obs2.	43
3.11	Phase resolved analysis results of the 4 variable parameters of Model A for Obs3.	44
4.1	Time evolution of variable parameters during pulse-on and pulse-off	51

List of Tables

2.1	Observational information for Swift/XRT and NuSTAR (FPMA and FPMB) observations of Swift J005139.2-721704 in November 2018.	16
2.2	Difference in the start time of Swift observation 00010977003.	20
2.3	Period search results for SXP 4.78 during the 3 observations of NuSTAR.	27
2.4	Time differences of NuSTAR FPMB and Swift XRT relative to each NuSTAR's FPMA t_0 for every observation.	28
3.1	List of models used in the spectral analysis	31
3.2	Best-fitting parameters of the 0.3-50 keV range of SXP 4.78 using <i>Model A</i>	34
4.1	Inner radius of the accretion disk of SXP 4.78.	48
4.2	Upper boundaries of the magnetic field of SXP 4.78.	49

Chapter 1

Introduction

1.1 Pulsars

A pulsar is as a rapidly rotating neutron star, a spherical compact object formed when a massive star, approximately 8 - 20 M_{\odot} explodes as a supernova, leaving its core as the remnant. A typical non-rotating neutron star has a mass of 1.1 M_{\odot} to 2.16 M_{\odot} (Rezzolla, Most, and Weih 2018) and a radius of approximately 10 km. Their average density reaches 10^{17} kg/m^3 , a similar order of magnitude to that of an atomic core at $2.3 \cdot 10^{17} \text{ kg/m}^3$. In combination with their small size, this causes the creation of a steep and deep gravitational well that can accelerate matter falling towards them to relativistic speeds. The small size of pulsars also results in exceptionally high spins, after the collapse of the parent star and because of the conservation of angular momentum. Their typical observed rotational periods range from a few seconds to hundreds (or even ~ 1000 s seconds), although there is an extreme class of pulsars with periods as short as 10^{-2} s . Since their first discovery in 1967 by Jocelyn Bell Burnell and Antony Hewish, humanity has observed more than 2000 pulsars (Skelly 2022)¹, with their magnetic fields ranging from $10^4 T - 10^{11}$ (Reisenegger 2003), approximately 9 to 16 orders of magnitude stronger than Earth's (at $2.5 \cdot 10^{-5} T - 6.5 \cdot 10^{-5} T$) (Finlay et al. 2010).

1.2 X-ray Binaries

An X-ray Binary System (XRB) is defined as a binary star system that is luminous in X-rays. The binary consists of two objects, a donor star, which is a normal or evolved star, and an accretor, a compact object that can be a white dwarf, a neutron star or a black hole. The different categories and sub-categories of XRBs depend on the type of the compact object as well as the mass of the donor star, as mentioned in (Reig 2011). These include, but are not limited to, High Mass X-ray

¹<https://www.nasa.gov>

Binaries, Low Mass X-ray Binaries and Be/X-ray Binaries.

In an X-ray Binary, when the two objects have small orbital separation, mass can move from the donor to the accretor, usually forming an accretion disk around the compact object, as it continues its path towards the accretor's surface. Due to the immense gravitational well of the accretor the matter gets accelerated to relativistic speeds and it is heated to temperatures of up to a few keV. The combination of this thermal radiation and non-thermal process in the accretion flow result in X-ray emission over a broad energy range from ~ 0.1 keV up to >100 keV in some cases. Under circumstances that are discussed later, this energetic matter gives off this energy as X-ray light.

1.2.1 High Mass X-ray Binaries

A High Mass X-Ray Binary System (HMXB) is defined as an X-ray Binary system consisting of a donor star with high mass, usually $> 10 M_{\odot}$. These donor stars typically fall into the categories of O, B, Be, or blue supergiant stars. If the compact object is a neutron star, HMXBs are classified into 3 sub-categories, Be/X-ray Binaries, Supergiant X-ray Binaries (SGXRBs) and Supergiant Fast X-ray Transients (SFXTs) (Negueruela et al. 2006), determined by the means that the gas is accreted onto the accretor. In Be/X-ray Binaries, the mass transfer occurs when the neutron star passes through a circumstellar disk created by the donor star, while in SGXRBs, the accretion is the result of strong stellar winds of the supergiant star.

1.2.2 Be/X-ray Binaries

A Be/X-Ray Binary (BeXRBs) is a sub-category of HMXBs and is defined as a Be star - neutron star pair, with the Be star being the donor and the NS the accretor. A Be star is a non-supergiant star with a spectral type of B that has Balmer emission lines in its spectrum. The Balmer spectral lines are caused by the light interacting with a thin equatorial gaseous disk (circumstellar disk), surrounding a common Be star. The disk forms when material is expelled from the star in an equatorial outflow because of its very fast rotation (Porter and Rivinius 2003). An example of a Be/X-ray Binary is shown in Figure 1.1.

1.3 Transient X-ray Pulsars

A Transient X-ray Pulsar is a pulsar, part of an X-ray binary system, that becomes an X-ray source for a short amount of time, hence the word 'transient'. In the case of the system pictured in Figure 1.1, the pulsar is considered a transient source. When it approaches the donor star, an outburst of X-rays can be observed

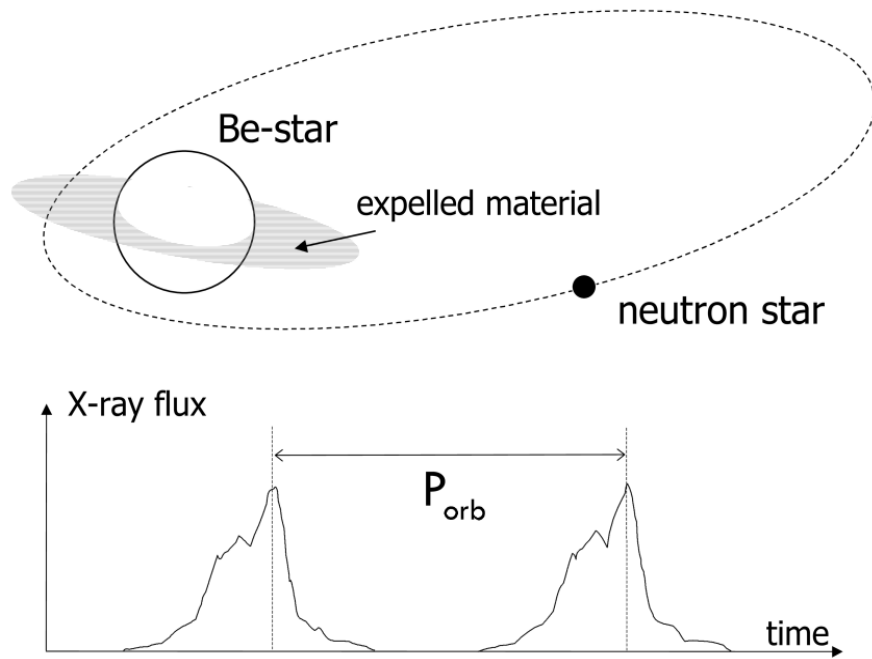


Figure 1.1: Schematic of a Be/X-ray Binary system, with the compact object orbiting the Be-star with an orbit period equal to P_{orb} . The orbit of the neutron star brings it close, or even inside of the circumstellar disk, resulting in an influx of observed X-rays with a period of P_{orb} as well (Tauris and van den Heuvel 2006).

from the system for a short period of time, usually between a few days and a few weeks, depending on size the circumstellar decretion disk. As the orbital separation increases, the accretion rate drops, resulting in lower X-ray luminosity. The accretion will remain low, or even zero, until the pulsar comes close to the donor star again, after completing a full orbit.

BeXRBs such as the one in Figure 1.1 produce X-rays of high luminosity only during their outbursts, when they accrete matter from their companion star. During the remainder of their orbit, it is difficult to acquire any information for the pulsar, so space telescopes that can observe such systems as soon as a sign of an outburst is detected, are vital for the study of transient X-ray sources.

1.4 Accretion

Accretion can be defined as the accumulation of matter onto an object. The matter is usually in a gaseous form and it can originate from a surrounding nebula, or a nearby companion star, such as in binary systems. The scale of accretion can vary greatly, from the accretion of dust around protoplanets in newly formed planet systems, to the center of massive galaxies where matter is accreted into

supermassive black holes resulting sometimes in the quasar phenomenon. In XRBs, accretion is responsible for fueling the X-ray emissions from the compact object, when matter escapes from the donor star and is captured by the gravitational well of the accretor, losing potential energy in the process.

1.4.1 Accretion in Binary Systems

When studying binary systems, we can observe three distinct types of accretion in nature:

1. Spherical Stellar Wind Accretion
2. Roche Lobe Accretion
3. Be-Star Accretion

Spherical stellar wind accretion is the accretion that we observe when the stellar wind of the donor star is captured by the gravity of the compact object. The most common cases of high stellar wind in stars are the luminous O and B stars (Kudritzki and Puls 2000). The accretion rate in this occasion is relatively small, compared with the other two types, but it can be enough to create an outburst, especially if the accretor is close to its companion. An example of stellar wind accretion is illustrated in Figure 1.2.

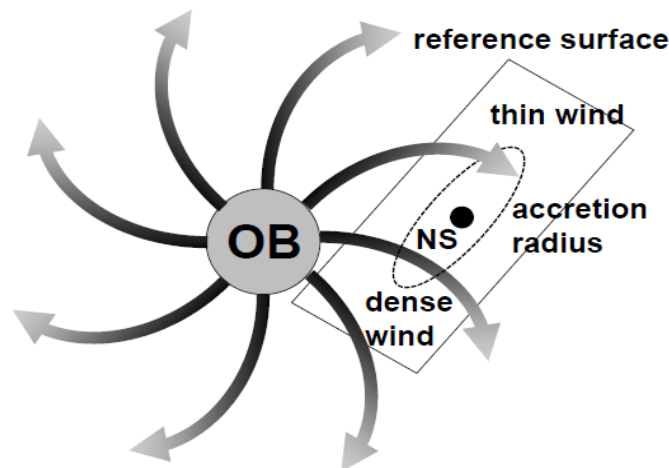


Figure 1.2: Schematic of a binary system consisting of a neutron star and an OB star. The stellar wind is depicted as arrows pointing outwards from the donor star. The density of the wind is decreasing as it moves away, so the closer the neutron star is to the donor star, the greater the accretion rate will be (Karino, Nakamura, and Taani 2019).

Roche Lobe Accretion is defined as the accretion that takes place when the gravitational wells of two objects come close enough for a Roche lobe to form, see Figure 1.3. This can be the result of an increase in the radius of the donor star, or the orbital decay of the system. The meeting point of the two lobes between the two objects, where the mass transfer occurs, is the Lagrange point 1 (L1).

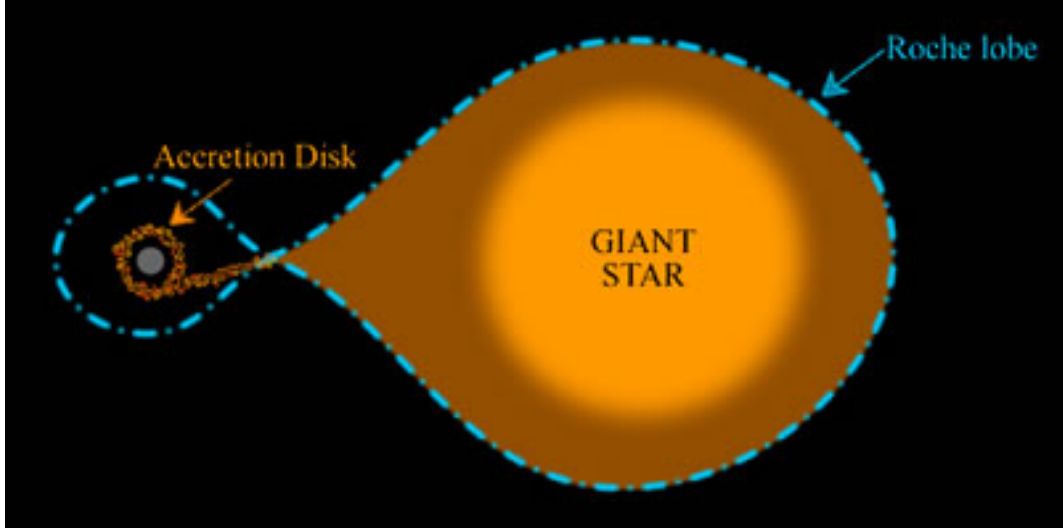


Figure 1.3: Illustration of a binary system where Roche lobe accretion is taking place. Due to the gravity of the accretor, the gas that originated from the surface of the donor star is attracted to the compact object. Following the Roche lobe, the matter creates an accretion disk around the accretor, where it then falls onto its surface. (Image credit: <https://astronomy.swin.edu.au/cosmos/r/roche-lobe>)

Finally, Be star accretion is defined as the accretion that occurs when a compact object passes through the circumstellar disk of a Be-star. This type of accretion is the reason behind the outbursts of BeXRBs (see Figure 1.1).

1.4.2 Accretion Disk

Accretion in Be/X-ray binary systems does not usually result in the formation of an accretion disk around the compact object. This is due to the low mass transfer rate and the strong magnetic field of the pulsar. The magnetic pressure from the magnetic field halts the radial flow of the gas and instead it channels it along the magnetic field lines. Despite that, evidence of accretion disks in Be/X-ray binaries have been found, such as in Christodoulou, Laycock, and Kazanas 2017. The existence of an accretion disk can cause the spin of the pulsar to increase or decrease, depending on the direction of rotation of the disk. For example, the spin down of neutron stars can be caused from a retrograde accretion disk (Christodoulou, Laycock, and Kazanas 2017).

1.4.3 Accretion Column

The accretion column forms from gas that is trapped by the magnetic field lines as it flows onto the pulsar. This disrupts the spherical or equatorial flow (accretion disk) of the gas and channels it along the magnetic field lines onto the poles forming a column of hot plasma. The turbulent flow of the gas in the accretion disk around the pulsar slowly drains the kinetic energy of the matter, causing it to reduce the radius of its orbit inside the disk, spiraling towards the center. The lowest possible orbit is called the Alfvén radius, where the kinetic energy density is equal to the magnetic energy density (Belenkaya, Khodachenko, and Alexeev 2015). When the gas reaches the Alfvén radius, it will follow the magnetic field lines and will arrive above the magnetic poles of the pulsar, moving parallel to the magnetic axis and reaching relativistic velocities, see Figure 1.4.

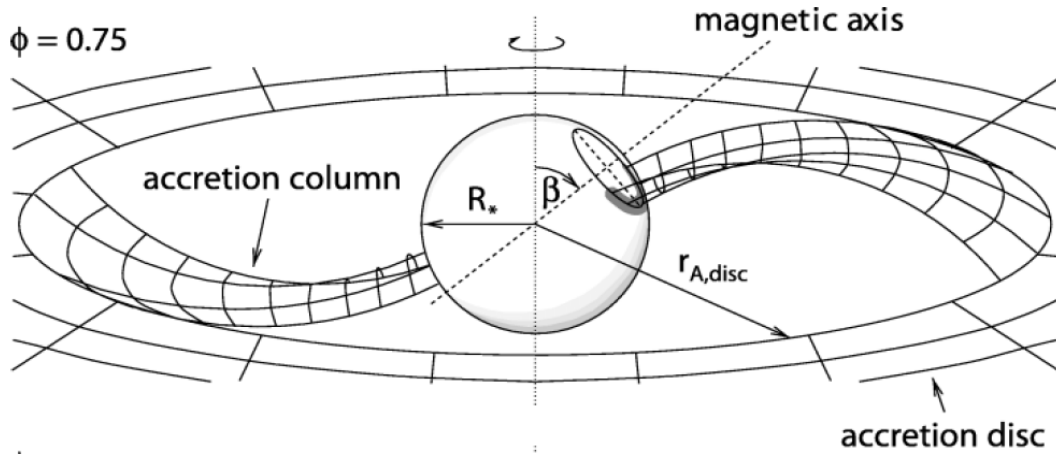


Figure 1.4: Schematic of an accretion disk around a pulsar and of the creation of the accretion columns on its north and south magnetic pole. The matter slowly loses kinetic energy and moves towards the pulsar. After reaching the Alfvén radius, here noted as $r_{A,disc}$, it follows the magnetic field lines and creates an accretion column on each magnetic pole (Galloway et al. 2001).

Continuing its path, the matter will accelerate from the higher parts of the accretion column towards the magnetic pole, see Figure 1.5. The supersonic speed of the fall will be reduced to subsonic speeds after the gas hits a standing shock that has been created from the balance of the in-falling material and the radiation pressure from the radiating matter underneath. Soft X-ray photons that are produced inside the accretion column get up-scattered to higher energies, due to the relativistic electron scatterings. These photons are thermal photons in nature (sometimes called seed photons) and they result in a blackbody distribution. The complete spectrum we observe from an accretion column is a combination of those blackbody photons with photons from cyclotron and bremsstrahlung radiation processes, as well as the up-scattered photons (e.g. Becker and Wolff 2007). An example of the combination of the aforementioned processes is presented in Figure 1.6.

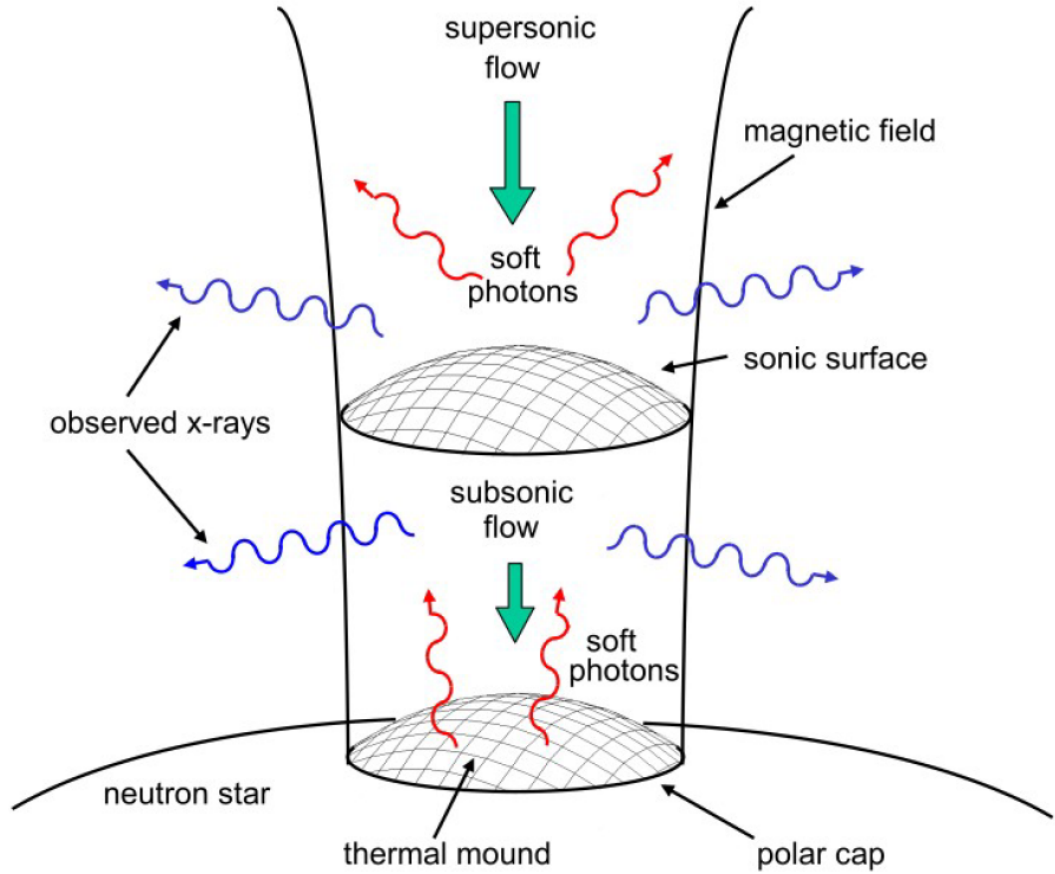


Figure 1.5: Schematic of an accretion column. The matter falls onto the magnetic pole as seen with the green arrow with a supersonic flow. After reaching the sonic surface it begins to slow down to a subsonic flow until it deposits at the thermal mound above the polar cap. Soft X-ray photons emitted at from the mound, with the red wave-arrows, increase their energy after inverse Compton scatterings that take place as the matter is falling with relativistic speeds. Then the energized hard X-ray photons, with the blue wave-arrows, escape from the sides of the column (Becker and Wolff 2007).

The rotation of a pulsar will influence the spectrum, because during one revolution, we observe the accretion column from different perspectives. For example, the accretion column does not have the same temperature throughout its structure, so when we observe it from an angle we expect different spectral shapes as a function of pulsar phase since we see different parts of the accretion column.

The photons escaping from the side of the accretion column make up the fan beam, while the radiation escaping from the top is defined as the pencil beam (see Figure 1.7). The fan beam is wider than the pencil beam, as it originates from a larger surface. Both beams can show variations during a spin period, depending on the viewing angle of the system. The narrow nature of the pencil beam makes it visible only if we observe the top of the accretion column, so we cannot observe it on spin phases which point it away from us. The variations on the fan beam

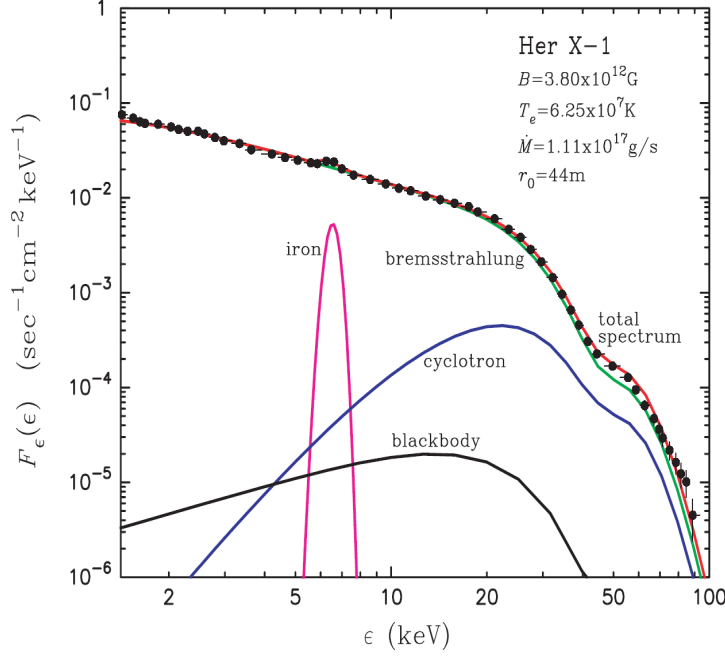


Figure 1.6: Theoretical column-integrated count rate spectrum of X-ray pulsar Her X-1. The different colored lines represent different processes resulting in the complete spectrum. Note that the Iron emission line originates from the accretion disk (Becker and Wolff 2007).

are caused by the obscuration of the side view of the accretion column from the pulsar itself.

1.5 Pulse Profile

The pulse profile of a pulsar is defined as the intensity of the radiation as a function of the pulsar rotational phase. It is calculated by folding a lightcurve over the pulsar rotational period. A diagram of a pulse profile showcases how the luminosity of the pulsar changes as a function of the phase of the period. The more bins a pulse profile has, the more accurately we can observe its shape, but that can result in a low number of counts.

Plotting the pulse profile of a pulsar in different energy ranges, we can understand the behaviour of the accretion column. By analyzing the pulse profile on soft X-rays, we usually have a relatively flat profile due to the fact that the majority of those photons originate from the accretion disk. Plotting the pulse profile in higher energies, pulsations like the ones in Figure 1.8 become more prominent, since they originate from the accretion column, that changes its view relative to us, as the pulsar spins.

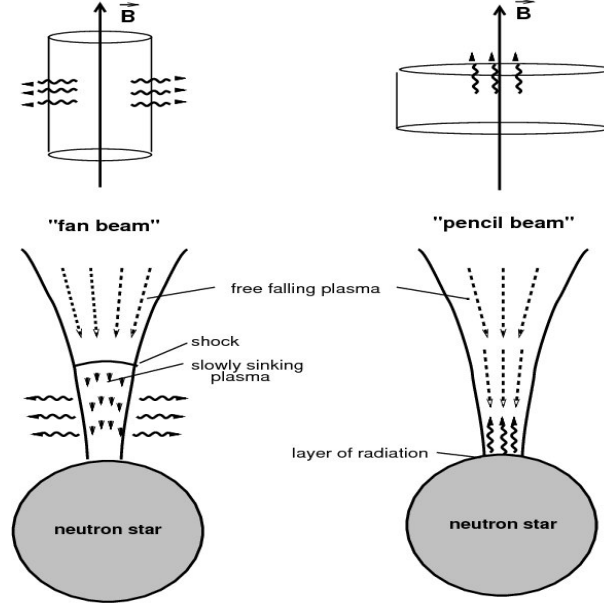


Figure 1.7: Schematic of pencil beam and fan beam. In the case of the fan beam, matter that is in free-fall collides with the shock created by the high radiation pressure from below, slowing down its decent, while forcing the surrounding photons to diffuse through the side, below the shock. In the case of the pencil beam, the radiation pressure is not high enough to create a shock, so the gas continues to fall towards the surface (Basko and Sunyaev 1976). There, after the effects of either the gas pressure, or Coulomb interactions, the resulting deceleration of matter will produce photons that will escape from the top of the accretion column (Becker, Klochov, et al. 2012). (Image credit: Schönherr et al. 2007)

1.6 Cyclotron Resonant Scattering Features

Cyclotron Resonant Scattering Features (CRSFs) are spectral features in the spectra of X-ray pulsars resulting from the interaction of the photons in the accretion columns with the electrons under the influence of the pulsars strong magnetic field. A CRSF can be observed as a fundamental absorption line approximately at 20 - 40 keV and possible harmonics at higher energies. The fundamental absorption line is caused by excited electrons that exist on the 1st Landau level, while the harmonics are the result of electrons that reside on higher Landau levels. The photons inside the accretion column are absorbed by these electrons, creating an absorption feature in the spectra of X-ray pulsars. The energy of the fundamental Cyclotron line is given by the following formula.

$$\epsilon_c = \frac{e B h}{2\pi m_e c} \quad (1.1)$$

where: B is the magnetic field of the neutron star, e is the charge of the electron, h is the Planck's constant, m_e is the mass of the electron and c is the speed of light. By substituting the physical constants we get Eq.1.2, where B_{12} is the magnetic

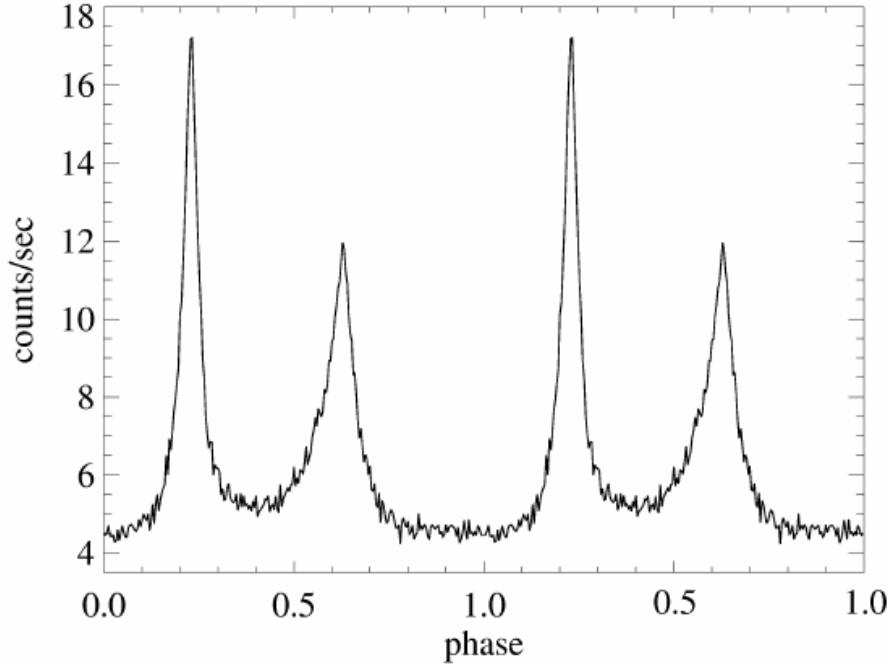


Figure 1.8: Pulse profile of the Crab nebula pulsar. We can differentiate the 2 peaks inside 1 rotation of the pulsar as the results of the 2 magnetic poles of the pulsar changing their viewpoints as it rotates (Kirsch et al. 2004).

field of the pulsar in units of 10^{12} G.

$$\epsilon_c \approx 11.57 B_{12} \text{ (keV)} \quad (1.2)$$

The importance of finding a cyclotron absorption line is great, since it allows us to measure directly the pulsar's magnetic field, a measurement which is very difficult to achieve otherwise. The energy of the CRSF can provide us with a direct way of calculating the magnetic field of the pulsar, by fitting an absorption line model component to the spectrum of the source, finding its energy and using Eq. 1.2.

1.7 Purpose of this Project

The source studied in this Thesis was a great opportunity to analyze an X-ray pulsar with a luminosity higher than the Eddington Luminosity. In stellar astrophysics, the Eddington Luminosity (otherwise known as Eddington Limit) is the maximum possible luminosity an object can radiate when is accreting matter spherically, when a balance of the forces of gravity and radiation pressure keep the system stable. Above the Eddington Luminosity, matter is ejected due to the high radiation pressure. In the case of X-ray pulsars, the accretion column does not have a spherical geometry, so the exceeding of the Eddington Limit refers to the

local conditions within the accretion column. In this case the release of radiation from the side of the cylinder, see Figure 1.7 in the fan beam case. The study of these high luminosity pulsars can give us insight on the dynamics of their accretion column, an environment that is considered considerably complex.

The aim of the project was to study a super-Eddington source and obtain information on the physical parameters of the accretion column using data acquired from X-ray space observatories. The analysis revolved around modeling both the soft and hard X-ray spectrum using appropriate models with physical and geometrical parameters of the accretion column. We also used models to study the temperature and size of the accretion disk around the neutron star. In addition, we extracted the pulse profile in different energy ranges and we used the bolometric luminosity of the source with the appropriate theory to impose an upper boundary on the magnetic field strength of the source. Finally, after finding the pulse period of the pulsar, we split the rotational phase into set parts and performed phase resolved spectroscopy on our search for changes of the accretion column parameters and for the possible existence of a CRSF.

Chapter 2

Observations and Methodology

2.1 The Target

In this Thesis we studied a HMXB inside the Small Magellanic Cloud (SMC) with the assigned name, Swift J005139.2-721704. The binary pair consists of a B1-2e type star, [M2002] SMC 20671 (Maravelias et al. 2018), and an X-ray pulsar, XTE 0052-723 or SXP 4.78. Its first discovery was in December of 2000 (Corbet, Marshall, and Markwardt 2001) during an outburst, observed with the Rossi X-Ray Timing Explorer (RXTE). Another outburst was observed in 2018, on November 19th, with a duration of approximately 12 days. The observations of Swift J005139.2-721704 during this last outburst were used for our project.

The spin period of the X-ray pulsar SXP 4.78 was measured by Corbet, Marshall, and Markwardt 2001 to be 4.782 ± 0.001 seconds. The HMXB is located in the Small Magellanic Cloud (SMC) at a distance of approximately 60.6 kpc (Graczyk et al. 2020). In Figure 2.1 we can see an optical image of the SMC with the HMXB of our study located in the middle.

A great number of X-ray pulsars have been discovered in the Large Magellanic Cloud (LMC) and the SMC. A reason for this is the fact that we do not observe the Magellanic Clouds through the thick parts of the disk of our Galaxy. Therefore, many observatories are on the lookout for new transient sources in both dwarf galaxies, attempting to acquire observational data as soon as an outburst occurs.

2.2 Observational Instruments

The instruments used for the data acquisition were the NuSTAR space observatory for studying the hard X-ray spectrum and the Neil Gehrels Swift space observatory for the soft X-rays.

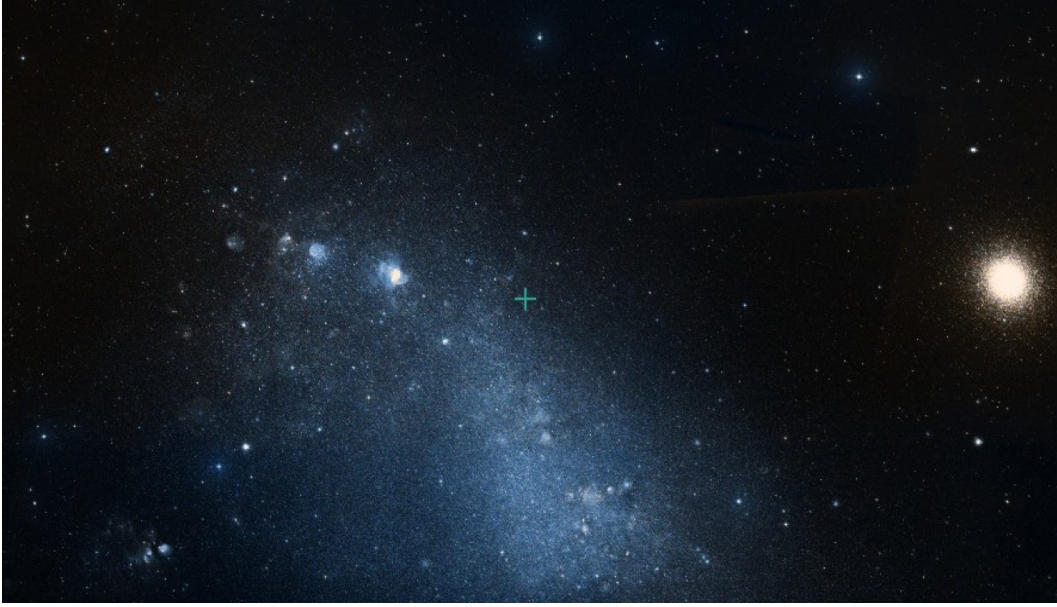


Figure 2.1: Optical image of the location of SXP 4.78 inside the SMC. The image is taken from the SDSS with a field of view of approximately $5^\circ \times 2.7^\circ$. The exact location of the HMXB is on the center of the image (green cross).

2.2.1 The NuSTAR Observatory

The Nuclear Spectroscopic Telescope Array (NuSTAR) is an X-ray space observatory capable of observing X-rays in the range of 3 - 78.4 keV (Harrison et al. 2013). NuSTAR was launched on the 13th of June 2013 marking the first time humanity could focus X-ray light from sources radiating higher than 10 keV. Its angular resolution is $18''$ (FWHM) and its temporal resolution is $2 \mu\text{s}$, making it a great tool for studying X-ray pulsars.

NuSTAR mainly consists of 3 parts, the focal plane with the detectors, a deployable mast and the optics, see Figure 2.2. It has 2 detectors with different focal plane modules, named FPMA and FPMB. The focal length of the telescope is approximately 10 meters, which is unavoidable, because of the way X-ray focusing works. The high energy X-rays cannot be reflected like less energetic light, such as optical. An X-ray hitting a common optical mirror will be absorbed and re-emitted as lower frequency light, losing its past information. X-ray mirrors use grazing incidence, with high angles of reflection, to direct the light to the detectors, hence the need for long optical path. This becomes even more important for hard X-rays where the grazing incidence needs to have even smaller angles.

2.2.2 The Neil Gehrels Swift Observatory

The Neil Gehrels Swift telescope is a space observatory consisting of three instruments, the Burst Alert Telescope (BAT), Ultraviolet/Optical Telescope (UVOT)

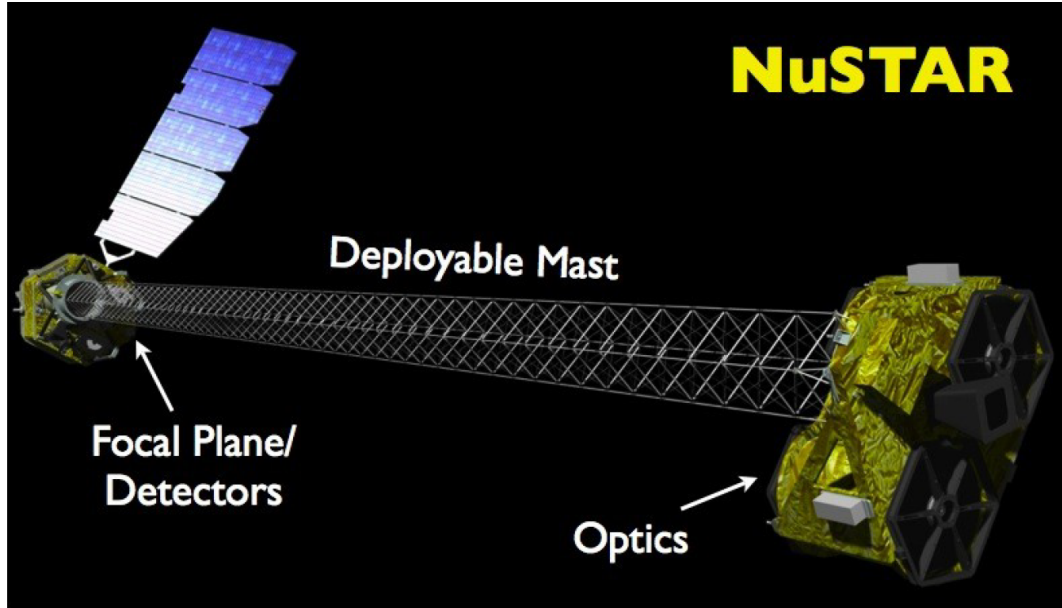


Figure 2.2: Depiction of the NuSTAR space observatory and its major parts. (Image credit: https://heasarc.gsfc.nasa.gov/docs/nustar/nustar_tech_desc.html)

and X-ray Telescope (XRT). It was launched on November 20th 2004 and although its main mission was to study gamma-ray bursts (GRBs) in the gamma-ray, X-ray, UV and visible part of the spectrum, it is now operated as a multi-wavelength observatory with a general purpose for any type of sources, especially astrophysical transients.

The Swift data we used for our analysis were acquired from the XRT instrument, which has an energy range of 0.2 - 10 keV (Gehrels et al. 2004). The resolution of the XRT is 18 arcsec resolution at half-power diameter, defined as the diameter within which half of the focused X-rays are enclosed¹.

2.3 Observations

After its last outburst in November 2018, the HMXB Swift J005139.2-721704 was simultaneously observed from NuSTAR and Swift in 3 separate occasions. Information regarding the observations of both space telescopes are presented in Table 2.1.

Plotting the count-rate as a function of time (Figure 2.4) we can see how the source changes its brightness in the span of those 13 days. The count-rates are measured after removing the contribution of the background as described in Section 2.4.1.

¹https://heasarc.gsfc.nasa.gov/docs/suzaku/prop_tools/suzaku_td/node9.html

²The NuSTAR count-rate value is the average value of the FPMA and FPMB detectors.

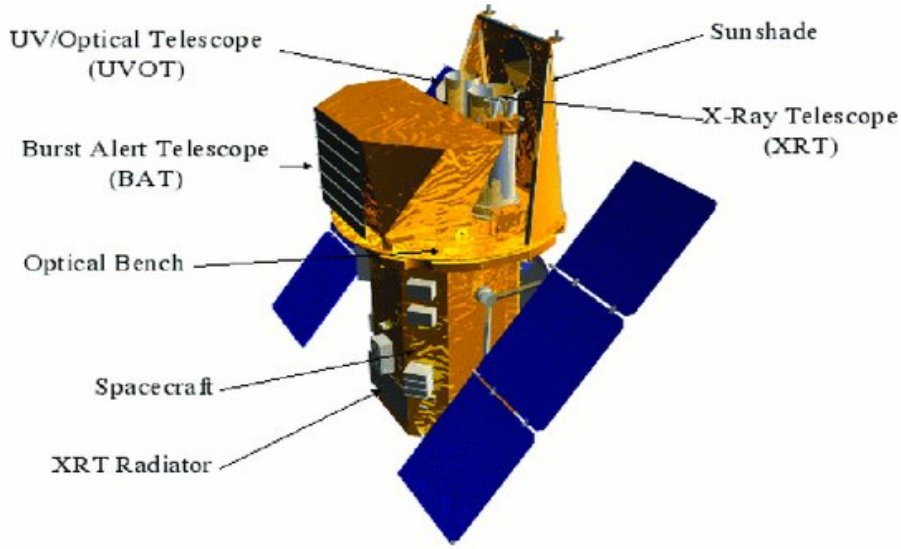


Figure 2.3: Depiction of the Neil Gehrels Swift space observatory with its major parts pinpointed (Saxena 2020).

Table 2.1: Observational information for Swift/XRT and NuSTAR (FPMA and FPMB) observations of Swift J005139.2-721704 in November 2018.

Observation ID	Start (UT)	End (UT)	Exposure (ks)	Count-rate ² (cps)
<i>Swift</i>				
00010977003	Nov 16 th 06:46	Nov 17 th 11:57	4.939	1.982
00010977004	Nov 25 th 10:30	Nov 25 th 14:08	5.987	2.837
00088816001	Nov 28 th 05:39	Nov 28 th 10:38	4.802	4.529
<i>NuSTAR</i>				
30361003002	Nov 15 th 19:00	Nov 17 th 13:57	74.470	4.883
30361003004	Nov 24 th 17:17	Nov 25 th 13:31	38.248	7.564
30361003006	Nov 27 th 07:58	Nov 28 th 21:40	73.170	8.341

2.4 Methodology

This section is dedicated to the data analysis of this project. After the data reduction, our analysis was split in the spectral analysis and the timing analysis. During the spectral analysis we used appropriate theoretical models to fit the data, while our timing analysis revolved around finding the pulse period of SXP 4.78 and splitting its rotation into parts in order to use the same theoretical models for spectral fitting in each phase.

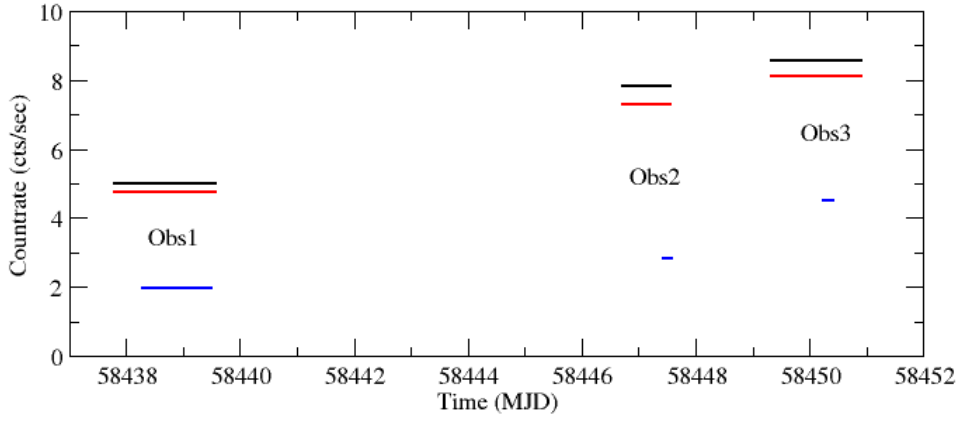


Figure 2.4: Count-rate (counts/s) as a function of time (MJD) during the 3 observational instances. Black: NuSTAR FPMA, red: NuSTAR FPMB, blue: Swift XRT. The observations of all 3 instruments take place during the showcased durations.

2.4.1 Data Reduction

NuSTAR Data Reduction

The NuSTAR data were acquired from the HEASARC Data Archive³ of NASA. The 3 observations of NuSTAR included all the necessary event files (.evt), as well as the orbit files of the telescope, holding information about the NuSTAR spacecraft. Each event file possesses information about every single photon that hit the FPMA and FPMB detectors. With the use of the version 6.26.1 of Heasoft⁴ and appropriate commands, such as "nupipeline" and "nuproducts", the data reduction was carried out in 3 main steps.

1. **Data Calibration**, where the calibration of the raw telemetry files (Level 0 science data) takes place, exporting them as Level 1a science data.
2. **Data Screening**, where the Level 2 science data are created, after appropriate use of filters and cleaning criteria, in addition to orbital and instrument parameters.
3. **Products Extraction**, where the final high-level scientific products (Level 3 science data) are exported, following their barycentric corrections. The products include, sky images, energy spectra, light-curves, Ancillary Response Files (ARF) and Redistribution Matrix Files (RMF).

Important files for the data reduction, like the region files for the source and the background selection, were selected using the Level 3 sky images and the

³<https://heasarc.gsfc.nasa.gov/docs/archive.html>

⁴<https://heasarc.gsfc.nasa.gov/docs/software/heasoft/>

SAOImageDS9⁵ software, see Figure 2.5. Each observation and each detector required different region files, based on the corresponding sky image. It should be noted that the parameter “binsize” was set to “0.01”, translated to a binning temporal resolution of 0.01 seconds. This was done to maximize the resolution of the pulse profiles.

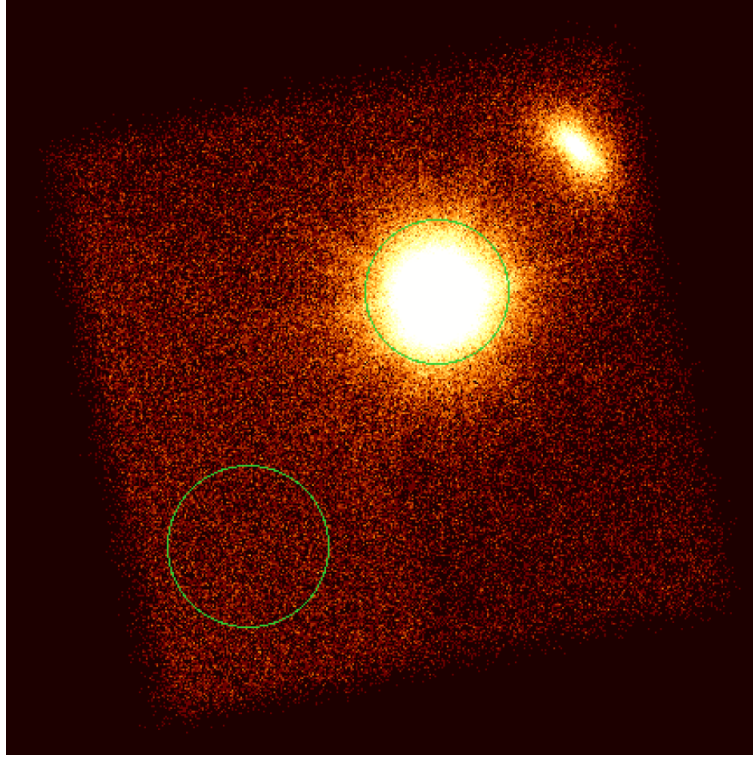


Figure 2.5: Region file selection for the source and background of Swift J005139.2-721704. The sky image was recorded by the FPMA detector of the observation 30361003002. The green circles define the region files for the source and background used for the data reduction. The object on the top right was recognized as SXP 91.1 (Monageng et al. 2019) using the XMM data and the SIMBAD Astronomical Database⁶.

Swift Data Reduction

The Swift data were also acquired from the HEASARC Data Archive. The data reduction process is similar to that for NuSTAR, with the 3 main stages carried out with the use of the “xrtpipeline” and “xrtproducts” commands. The Swift telescope observed SXP 4.78 with 2 different modes, the Photon Counting mode (PC) and the Windowed Timing mode (WT). The PC mode extracts a 2-dimensional image of the object, but it has a 2.5 second time resolution. The WT mode exports an 1-dimensional image, but it has a time resolution of 1.8 ms, making it great for pulsars⁷. Observations 00010977003 and 00010977004 were performed using

⁵<https://sites.google.com/cfa.harvard.edu/saoimageds9/home>

⁶<http://simbad.u-strasbg.fr/simbad/>

⁷<https://www.swift.ac.uk/analysis/xrt/modes.php>

the WT mode, see Figure 2.7, while observation 00088816001 was performed with both PC, see Figure 2.6 and WT mode. Finally, we applied a filter for the Grade value of the detected events on the WT mode observations, extracting only the Grade 0 data.

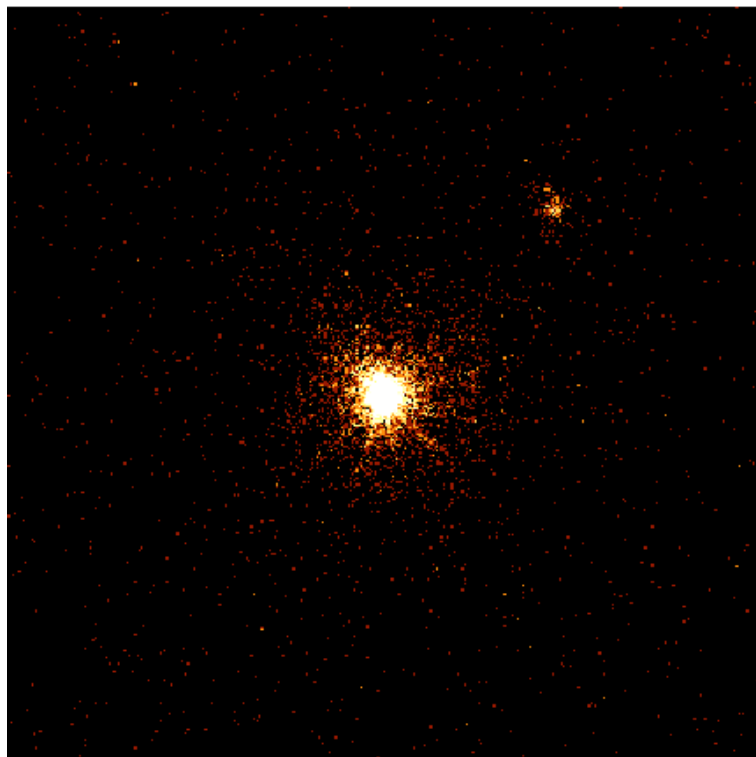


Figure 2.6: Sky image of SXP 4.78 from Swift observation 00088816001 using the PC mode. The object on the top right is SXP 91.1.

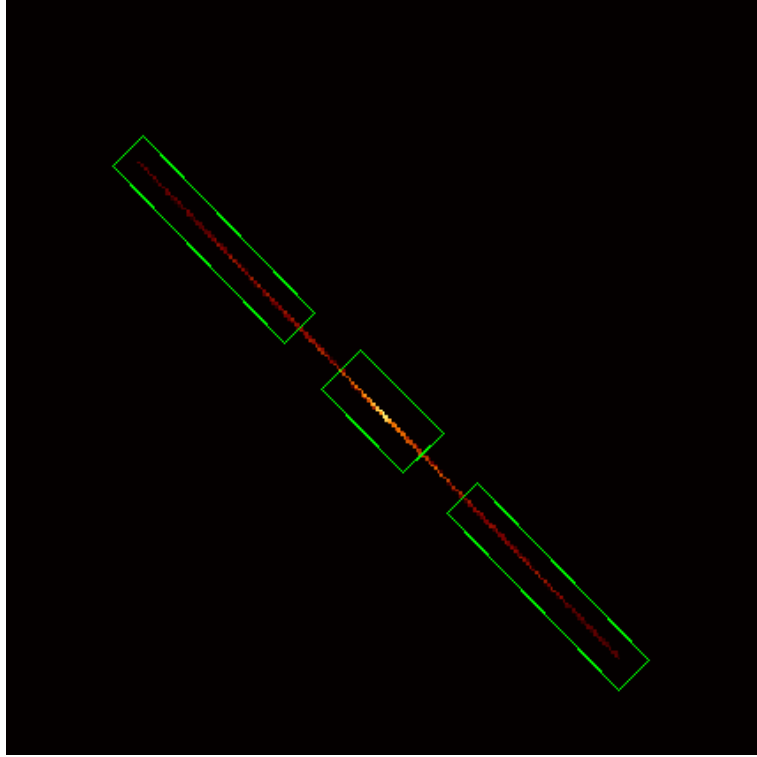


Figure 2.7: Sky image of SXP 4.78 from Swift observation 00010977004 using the WT mode and selected regions for the source and the background. The central parallelogram is the source region file and the other 2 parallelograms on its sides are the combined region file for the background.

Observation 00010977003 was performed using 5 different roll angles. This resulted in the need for 5 different extractions optimized for each roll angle in order to acquire the final data. The angles are presented in Table 2.2. Note that the products from angle a5 were flagged by the program as not reliable, so they were ignored.

Table 2.2: Difference in the start time of Swift observation 00010977003.

Angle Name	Angle (deg)	Start Time ⁸ (s)	Time Difference ⁹ (s)
a1	219.74	564043512.016714	0
a2	224.0965	564055650.129689	12138.112975
a3	225.303	564090256.049916	46744.033202
a4	219.5975	564146989.998293	103477.981579
a5	215.6715	-	-

⁸The start time are in reference to the Swift $t = 0$ at 51910 MJD.

⁹Relative to the angle a1.

Pile-up check for the Swift Observation 3

The Swift Observation with ID 00088816001, the only Swift observation performed using the PC mode, was examined for photon pile-up. Pile-up is defined as the overlapping charge distributions of multiple photons registered in the same CCD readout. When the probability of overlapping events is significant we observe pile-up in our data, making them non-reliable, since multiple photons are counted as single events with higher energy, resulting in the source appearing less luminous and with a harder spectrum.

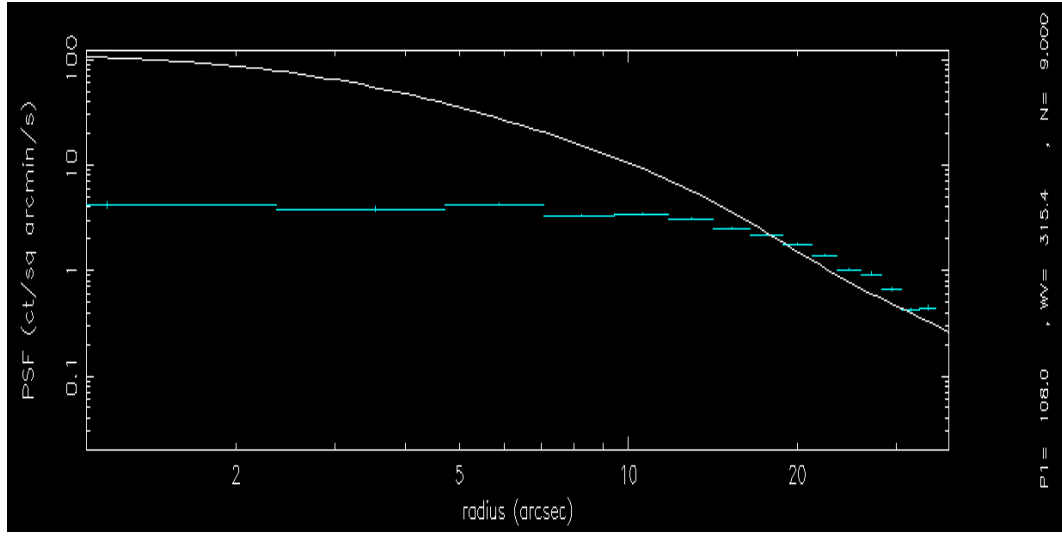


Figure 2.8: Pile-up modeling of Swift PC mode observation 00088816001. The observational data are represented by the cyan points and the model by the white continuous line.

The process of pile-up check requires the extraction of the radial profile which is compared against the Point Spread Function (PSF). The PSF is modelled as a King profile and a Gaussian component, which are fitted to the data (see Figure 2.8). The model is given by Eq. 2.1, where $W \sim 0.075$, $\sigma \sim 7.42$, $r_c \sim 3.72$ and $\beta \sim 1.31$ ¹⁰.

$$PSF(r) = W \exp[-r^2/(2\sigma^2)] + (1 - W)[1 + (r/r_c)^2]^{-\beta} \quad (2.1)$$

Noticing the significantly reduced intensity in the core of the source in comparison to the PSF model between our data and the model fit, we conclude that the Swift PC mode data of observation 00088816001 are piled-up, hence we cannot use them in our analysis. More specifically, the source appears approximately 10 times less luminous than it should be.

¹⁰<https://www.swift.ac.uk/analysis/xrt/pileup.php>

2.4.2 Spectral Analysis

After extracting the spectra for every observation and both telescopes we grouped them using the "grppha" command. The grouping ensured a minimum of 20 counts per bin so that chi squared statistics could be used. Using the XSPEC software¹¹ we imported the grouped spectra and begun the modeling procedure, utilizing a combination of theoretical models available in the XSPEC model database¹². In Figure 2.9 we present the complete spectra of the 3 observational instances from NuSTAR and Swift. After noticing the noise above ~ 50 keV and taking into account the effective ranges of both instruments, we decided to ignore all the Swift data outside of the 0.3 keV - 8 keV range, as well as all the NuSTAR data outside of the 4 keV - 50 keV range. The final spectra are presented in Figure 2.10.

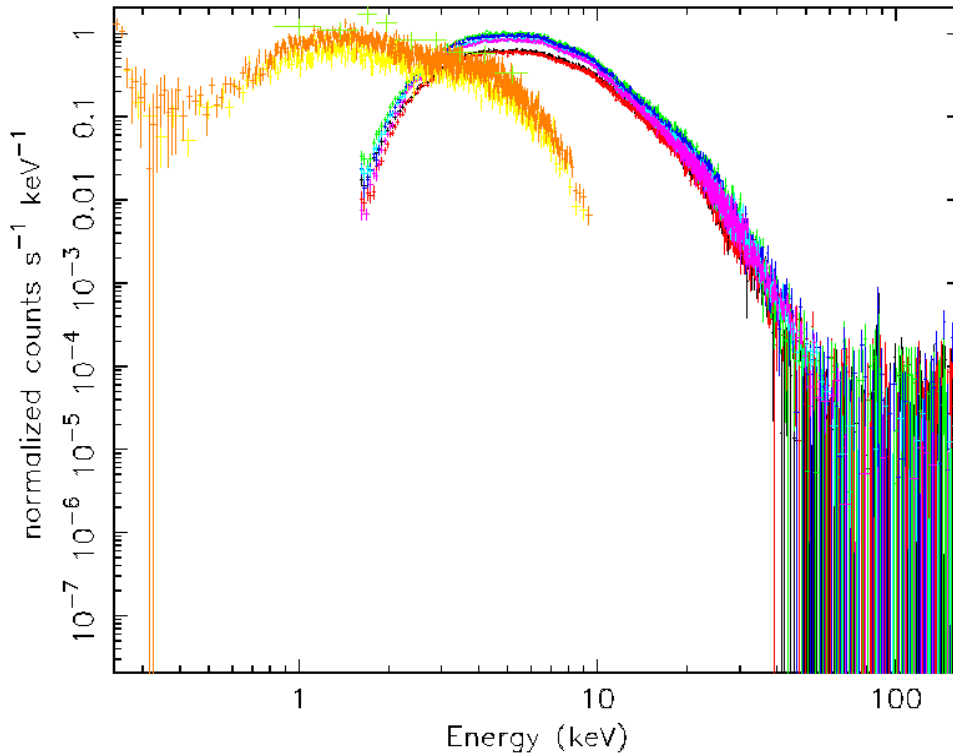


Figure 2.9: Initial spectrum of SXP 4.78 from every observational instance from 0.1 keV - 150 keV. Black and red: NuSTAR Obs1 FPMA and FPMB respectively. Green and blue: NuSTAR Obs2 FPMA and FPMB respectively. Cyan and pink: NuSTAR Obs3 FPMA and FPMB respectively. Yellow, orange and light green: Swift Obs1, Obs2 and Obs3 respectively.

Two spectral components were the same for all the spectra we considered. First we include a multiplicative constant parameter *const.*, frozen on the first dataset and left free to vary for the rest in order to account for calibration variations

¹¹<https://heasarc.gsfc.nasa.gov/xanadu/xspec/>

¹²<https://heasarc.gsfc.nasa.gov/xanadu/xspec/manual/Models.html>

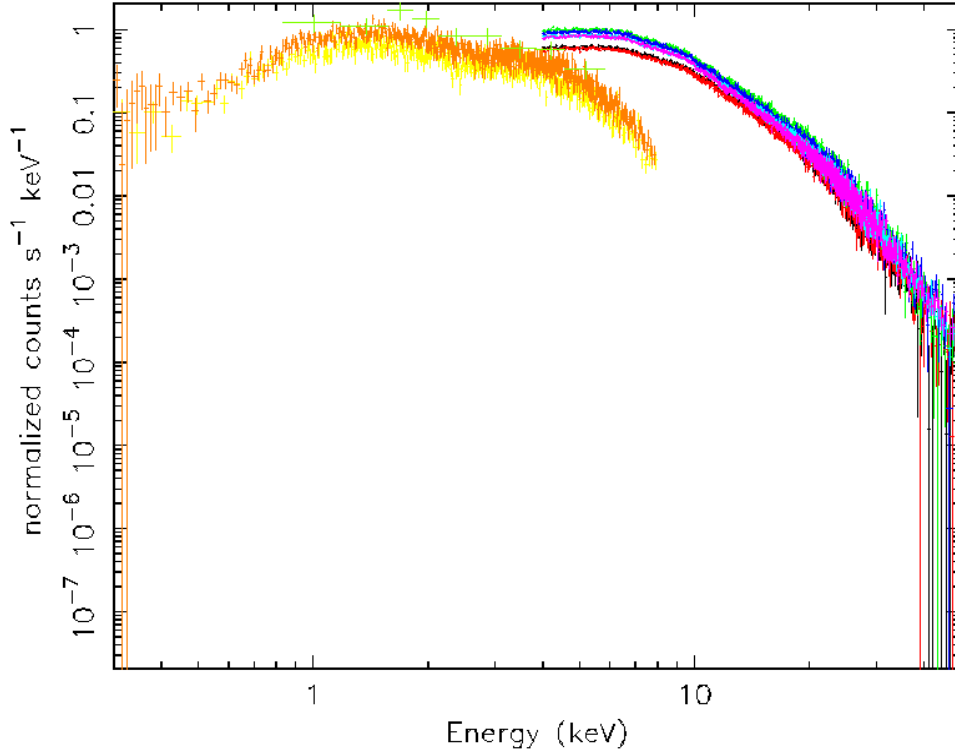


Figure 2.10: Final spectrum of SXP 4.78 from every observational instance from 0.3 keV - 50 keV, after the appropriate ignore of data. The colors are similar with Figure 2.9.

between the different instruments. The Tuebingen-Boulder ISM absorption model *tbabs* was also used on every model (Wilms, Allen, and McCray 2000). The model takes into account the gas, molecules and grains of the Interstellar Medium (ISM) and calculates the absorption cross-section for X-ray photons. The one parameter of *tbabs* is the equivalent hydrogen column in units of (10^{22} atoms cm^{-2}), nH .

The confidence ranges of every value in this thesis was calculated using $\Delta\chi$ statistics ($\Delta\chi = 2.706$, corresponding to a 90% confidence region). Next we discuss the individual model components used in our analysis. Initially, we begun with $const \cdot tbabs \cdot compmag$ (**Model O1**) and $const \cdot tbabs \cdot (compmag + diskbb)$ (**Model O2**), but after examining their residuals we arrived at the final models $const \cdot tbabs \cdot (compmag + diskbb + gauss)$ (**Model A**) and $const \cdot tbabs \cdot (compmag \cdot gabs + diskbb + gauss)$ (**Model B**).

Compmag

The *compmag* component describes the spectrum of an accretion column formed on top of a magnetic pole of a pulsar, based on (Becker and Wolff 2007). It utilizes the solution of the radiative transfer equation, after taking taking into account

thermal and bulk Comptonization processes, as well as cyclotron, bremsstrahlung and black-body emission. (Farinelli et al. 2012). The parameters of the model are as follows.

- par 1. **kT_{bb}** : The temperature of the seed photons of blackbody emission in keV.
- par 2. **kT_e** : The temperature of the electrons inside the accretion column in keV.
- par 3. **τ** : The vertical optical depth of the accretion column. The electron cross-section is defined as 10^{-3} of the Thomson cross-section.
- par 4. **η** : If $\text{betaflag} = 1$, then describes the index of the velocity profile for increasing velocity towards the pulsar.
- par 5. **β_0** : Terminal velocity of the accreting matter at the neutron star surface in units of the speed of light “c”.
- par 6. **r_0** : The accretion column radius in Schwarzschild radii of the pulsar
- par 7. **A** : The albedo at the surface of the pulsar. It remained frozen at 10^{-3} .
- par 8. **betaflag** : It was set to “1”, resulting in a velocity profile of

$$\beta(z) = \beta_0 \left(\frac{Z_0}{Z_S} \right)^\beta \left(\frac{Z_S}{Z} \right)^{-\eta}$$

- par 9. **norm.** : A normalization factor equal to R_{km}^2/D_{10}^2 , where R_{km} is the accretion column radius in km and D_{10} is the distance to the pulsar in units of 10 kpc.

Gauss

The Gauss component describes a profile of a simple Gaussian line, as seen in Eq. 2.2.

$$A(E) = K_g \frac{1}{\sigma\sqrt{2\pi}} \exp\left[-\frac{(E - E_l)^2}{2\sigma^2}\right] \quad (2.2)$$

- **E_l** : The energy of the Gaussian line in keV.
- **σ** : The width of the Gaussian line in keV.
- **K_g** : A normalization factor in units of $\text{photons}/\text{cm}^{-2}/\text{s}$, giving the total intensity of the source.

Diskbb

The diskbb model describes emission from an accretion disk combining multiple blackbody components (see e.g. Mitsuda et al. 1984). The parameters of diskbb are listed below.

- T_{inn} : An effective temperature at the inner disk radius R_{inn} in keV.
- **norm**: A normalization factor equal to $(r_{in}/D_{10})^2 \cos \theta$, where r_{in} the apparent radius of the inner part of the accretion disk and D_{10} the distance to the source in units of 10 kpc¹³.

The apparent inner radius r_{inn} is related to the true inner radius R_{inn} using Eq.2.3, from Kubota et al. 1998. Note that $\kappa \sim 1.7 - 2.0$ (Shimura and Takahara 1995) and $\xi = \sqrt{\frac{3}{7}} \cdot \left(\frac{6}{7}\right)^3$ (Kubota et al. 1998).

$$R_{inn} = \xi \cdot \kappa^2 \cdot r_{inn} \quad (2.3)$$

Gabs

The gabs component was tried for the search of a possible cyclotron absorption line (CRSF). CRSFs do not present an exact Gaussian profile, but the gabs can be an acceptable approximation (Tsygankov and Lutovinov 2005). The functional form of the model is given by Eq.2.4, with its parameters below.

$$M(E) = \exp\left[-\left(\frac{d}{\sigma\sqrt{2\pi}}\right)\exp\left[-\frac{1}{2}\left(\frac{E - E_l}{\sigma}\right)^2\right]\right] \quad (2.4)$$

- E_l : The energy of the line center in keV.
- σ : The width of the line in keV.
- d : The line's depth, where the optical depth at the center of the line is $(d/\sigma)/\sqrt{2\pi}$.

2.4.3 Timing Analysis

The timing analysis of SXP 4.78 consisted of the measurement of its pulse period in each observation and the binning of the events in appropriate phases in order to perform spectral modeling to each phase.

¹³For $\theta = 0$, we are looking at the disk face-on.

Pulse Period Search

The process of period search requires the lightcurve files from the products of the data reduction. The commands "powspec", "efsearch" and "efold" of the XRONOS software¹⁴ were used for the analysis. The "powspec" command creates a frequency spectrum of the lightcurve, where we can extract an initial value for the spin period, see Figure 2.11. The "efsearch" command requires an initial guess value for the period to refine the final result. This initial guess was the period measured from the power spectrum. The final values are presented on Table 2.3. Note that the Swift data could not provide a reliable constraints on the pulse period due to the smaller number of counts and the lower pulse fraction in the soft X-ray band.

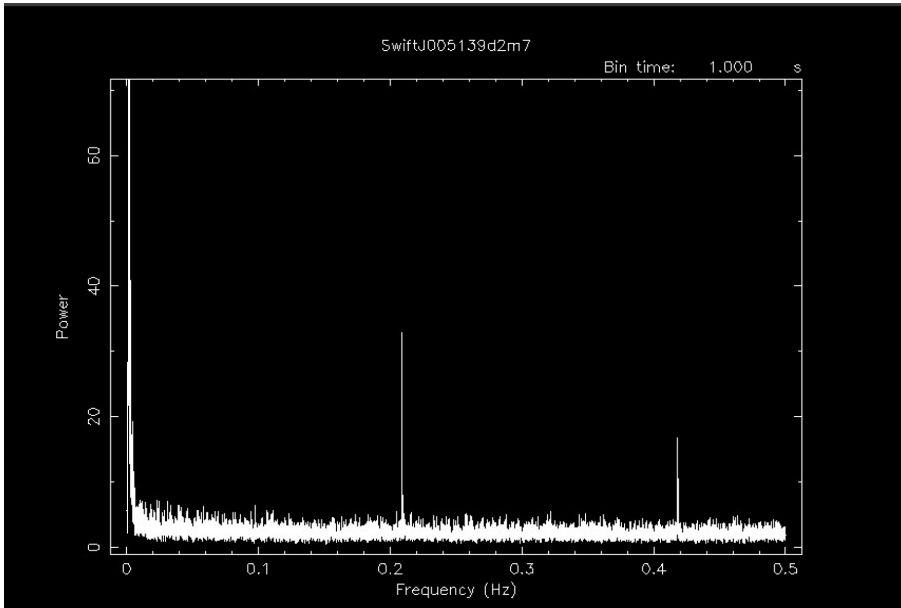


Figure 2.11: Power spectrum of the lightcurve of NuSTAR FPMA observation 30361003002. The initial guess was selected at ~ 0.209 Hz, or ~ 4.78 s.

¹⁴<https://heasarc.gsfc.nasa.gov/xanadu/xronos/xronos.html>

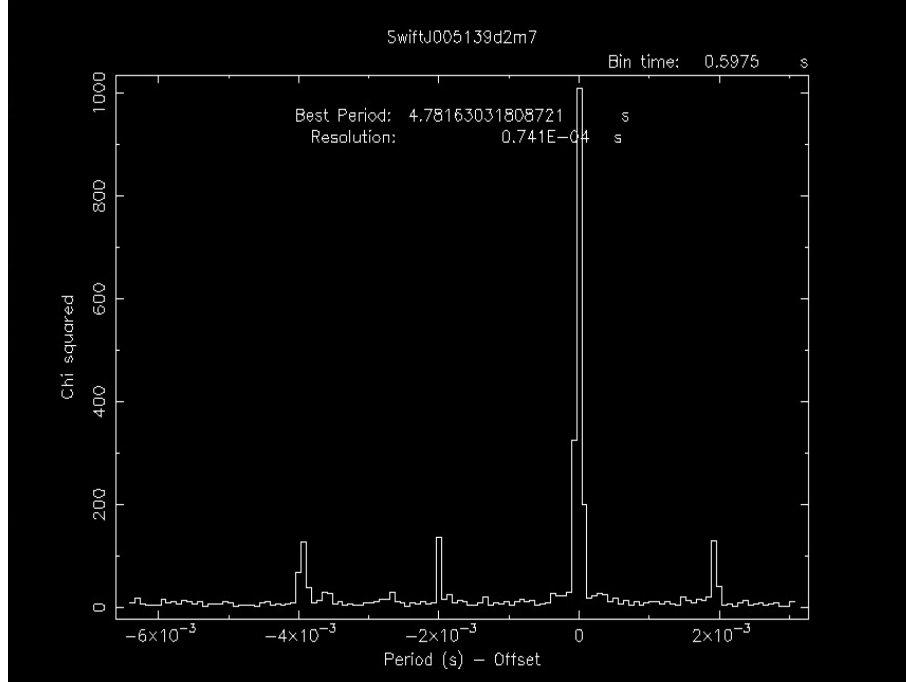


Figure 2.12: Chi-squared - period offset diagram of the lightcurve NuSTAR FPMA observation 30361003002.

Table 2.3: Period search results for SXP 4.78 during the 3 observations of NuSTAR.

Observation ID	Period (s)	
	FPMA	FPMB
30361003002	$4.7816^{+0.0002}_{-0.0002}$	$4.7816^{+0.0002}_{-0.0002}$
30361003004	$4.7816^{+0.0002}_{-0.0002}$	$4.7816^{+0.0002}_{-0.0002}$
30361003006	$4.7816^{+0.0002}_{-0.0001}$	$4.7816^{+0.0002}_{-0.0001}$

Our results for the spin period come in agreement with both Corbet, Marshall, and Markwardt 2001 and Semena et al. 2019.

Phase Binning

The phase binning process required an absolute time reference for both NuSTAR and Swift. The pulsar has a period of 4.7816 seconds, so the time accuracy of the phase binning is vital, otherwise it is possible that phase resolved spectra extracted from data from one telescope do not correspond to the same phases for spectra of the other telescopes. For every one of the 3 instances that SXP 4.78 was observed we set the $T_{\text{init.}} = 0$ at the reference time of NuSTAR's FPMA detector. It should be noted that because of the Swift mission start time of nearly 9 years earlier, we need to take into account 2 leap seconds that were introduced in the meantime¹⁵. The time differences that were taken into account are presented in Table 2.4. The

¹⁵<https://www.nist.gov/pml/time-and-frequency-division/time-realization/leap-seconds>

time offsets were calculated to the Swift observations taken simultaneously with the NuSTAR observations and are registered with the corresponding NuSTAR observation. Note that we do not attempt to define the absolute phase of the different observations since these offsets can be calibrated by cross-registering the pulse profiles. Finally, the Swift observation 0088816001 did not have enough photons during its WT mode observation to proceed with a phase resolved analysis.

Table 2.4: Time differences of NuSTAR FPMB and Swift XRT relative to each NuSTAR's FPMA t_0 for every observation.

Instrument	Start Time (s)		
	Obs1 ¹⁶	Obs2	Obs3
NuSTAR (FPMB)	-0.0292002	-0.0211766	-0.022502
Swift (XRT)	42327.021955	61922.433478	-
	54465.134930		
	89071.055157		
	145805.003534		

For each observation we calculate pulse profiles in 0.1 phase intervals. The splitting was performed using Eq.2.5, where P is the pulse period, T the time of each event, $T_{init.}$ is the start time we defined by the NuSTAR's FPMA start time and the time differences in Table 2.4 and $\%$ is the mod function. An indicative pulse profile is shown in Figure 2.13. After examining the number of counts in all phase bins of the 3 observational instances, we decided to group selected bins together in order to increase the signal-to-noise ratio and ensure higher quality phase resolved spectra. Low intensity bins were grouped at similar, adjacent phase bins. The final grouped phase bins are presented in Chapter 3.

$$\frac{(T - T_{init}) \% P}{P} \quad (2.5)$$

¹⁶The Swift XRT 4 different start times represent the 4 roll angles of observation 00010977003.

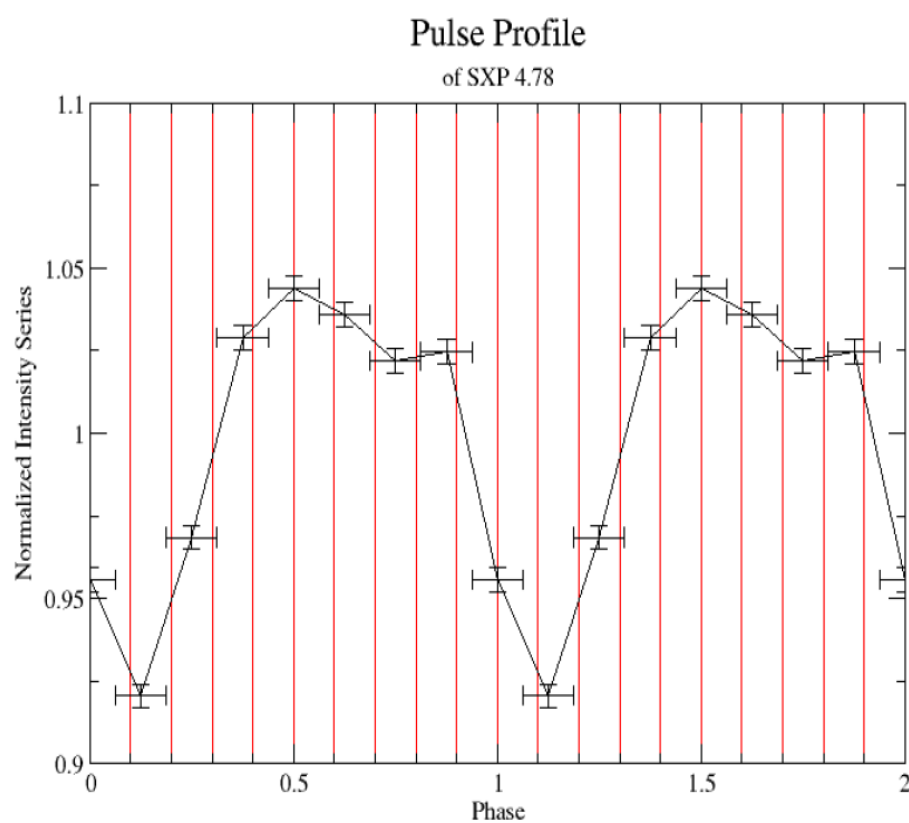


Figure 2.13: The pulse profile of Obs1 NuSTAR FPMA, showing the 10 phases in which the pulse profile is calculated.

Chapter 3

Results

In this chapter we present the result of the analysis. The chapter is split into 3 major sections, the results from the phase averaged analysis, the presentation of the pulse profile and the results from the phase resolved analysis.

3.1 Phase Averaged Analysis

In this section, the results of the phase averaged analysis are presented. In the first subsection we present the spectral fits of **Model O1** and **Model O2** and we explain the reason we decided to discard them for **Model A**. The next subsection is dedicated to the fitting of the data of all 3 observational instances with **Model A**. In Table 3.1 we present the models used in the spectral analysis.

Table 3.1: List of models used in the spectral analysis

Model Name	Expression
<i>Model O1</i>	$const \cdot tbabs \cdot compmag$
<i>Model O2</i>	$const \cdot tbabs \cdot (compmag + diskbb)$
<i>Model A</i>	$const \cdot tbabs \cdot (compmag + diskbb + gauss)$
<i>Model B</i>	$const \cdot tbabs \cdot (compmag \cdot gabs + diskbb + gauss)$

3.1.1 Initial Models

The spectrum of X-ray pulsars has a powerlaw-like shape, described adequately by the Becker & Wolff model of "compmag". We decided to begin the modeling procedure by the simple **Model O1**. The resulting fit is presented in Figure 3.1. Noticing the significant residuals at the soft X-rays we added the component "diskbb" to fit the spectrum of an accretion disk which is expected to be around the neutron star of high accretion rates. In Figure 3.2 we present the resulting fit

of *Model O2*. Finally, a small bump can be seen around 6.4 keV in the residuals of Figure 3.2, an effect of an Iron emission line we expect to observe, so we added the final component "gauss", creating *Model A*.

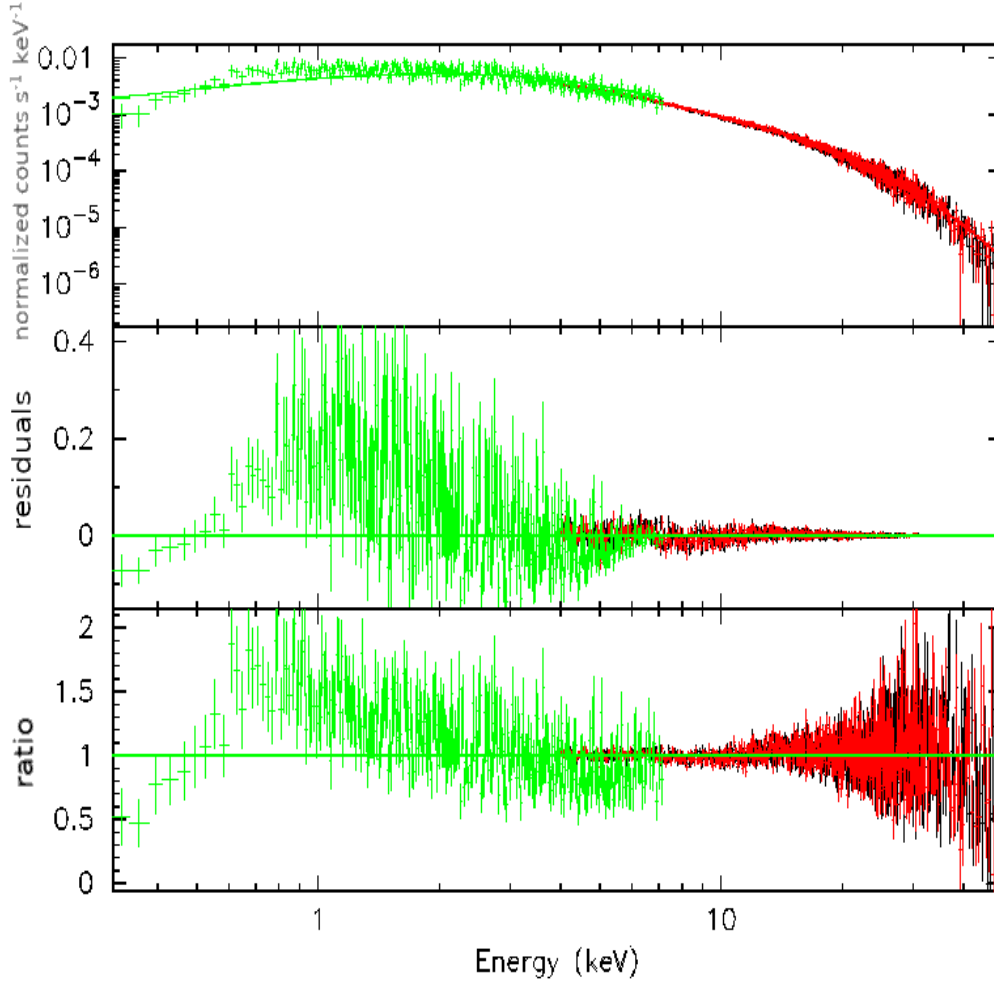


Figure 3.1: From top to bottom: (a) Energy spectrum of Observation 1 with the Model O1 best fit. (b) Residuals of Model A best fit in normalized counts $\text{s}^{-1} \text{keV}^{-1}$. (c) Ratio of Model A best fit. The green points show the Swift data and black and red points show the data from the FPMA and FPMB NuSTAR detectors respectively. The lines show the best fit models convolved with the instrument response.

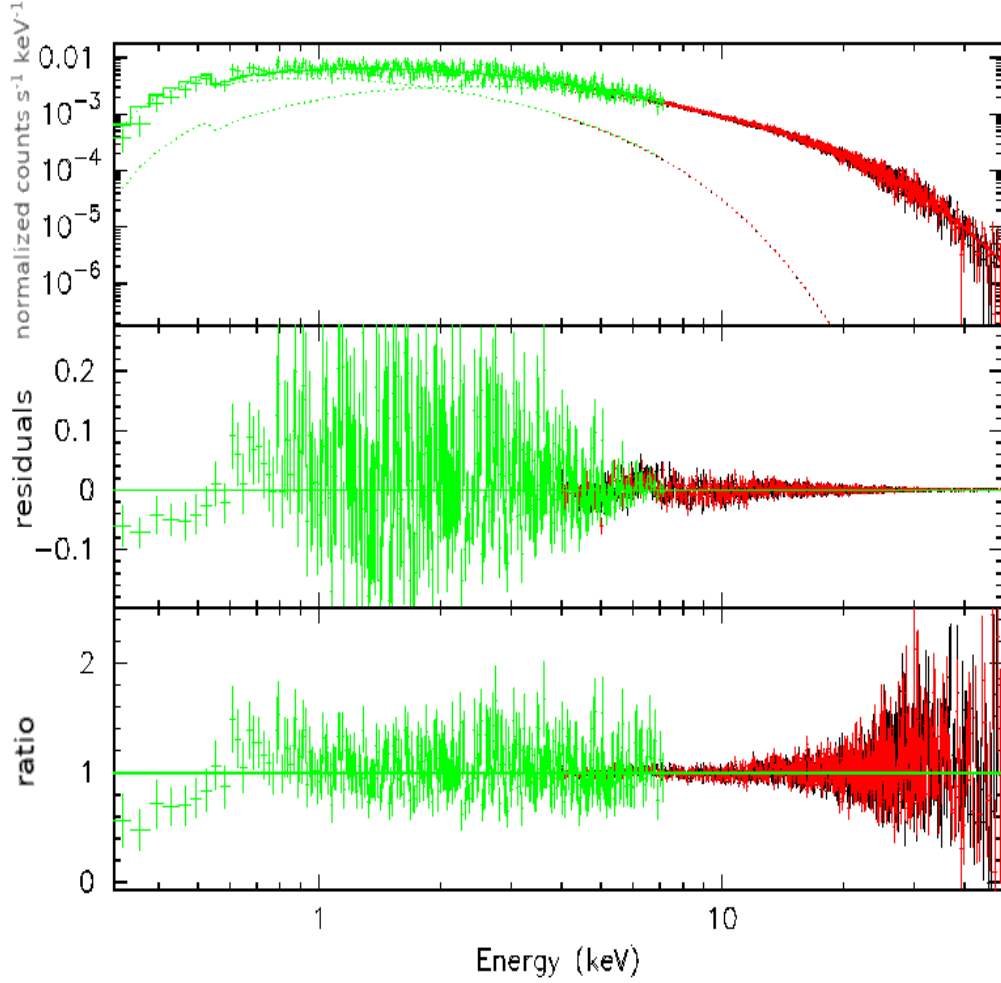


Figure 3.2: From top to bottom: (a) Energy spectrum of Observation 1 with the Model O2 best fit. We can differentiate the 2 modeling components of compmag and diskbb with the dotted lines. (b) Residuals of Model A best fit in normalized counts s⁻¹ keV⁻¹. (c) Ratio of Model A best fit. The green points show the Swift data and black and red points show the data from the FPMA and FPMB NuSTAR detectors respectively. The lines show the best fit models convolved with the instrument response.

3.1.2 Model A Fitting

Phase averaged spectra (i.e. from the entire pulse) are fitted using Model A and Model B. In Table 3.2 we present the best-fitting parameters of Model A. The bolometric luminosity was calculated using Eq.3.1, where D is the distance to the source and F_{bol} is its bolometric flux.

$$L_{bol} = F_{bol} \cdot 4\pi D^2 \quad (3.1)$$

Following Table 3.2, we present the data with the fitted model, the model's residuals and the model ratio of all 3 observational instances, see Figures 3.3, 3.4 and 3.5.

Table 3.2: Best-fitting parameters of the 0.3-50 keV range of SXP 4.78 using *Model A*.

Observation ID	Obs1	Obs2	Obs3
$Flux_{bol}^1$, $10^{-10} erg/cm^2/s$	3.2942	4.8659	5.6378
L_{bol} , $10^{38} erg/s$	1.4475	2.1381	2.4772
N_H , $10^{21} cm^{-2}$	1.6 ± 0.2	$1.6^{+0.1}_{-0.2}$	2^{+2}_{-1}
T_{in} , keV	1.435 ± 0.008	1.9 ± 0.2	$1.94^{+0.06}_{-0.1}$
$norm_{diskbb}$	0.57 ± 0.01	$0.35^{+0.1}_{-0.05}$	0.48 ± 0.06
kT_{bb} , keV	1.211 ± 0.005	1.2 ± 0.1	1.3 ± 0.1
kT_e , keV	3.57 ± 0.01	$3.7^{+0.6}_{-0.4}$	$4.45^{+0.03}_{-0.2}$
τ	1.024 ± 0.004	$0.95^{+0.1}_{-0.05}$	$0.84^{+0.03}_{-0.04}$
η	0.37 ± 0.03	$0.8^{+0}_{-0.8}$	$0.6^{+0.3}_{-0.4}$
β_0	0.08 ± 0.01	$0.11^{+0.05}_{-0.06}$	$0.02^{+0.04}_{-0.02}$
r_0	$0.40^{+0.04}_{-0.03}$	$0.6^{+0}_{-0.6}$	$0.6^{+0}_{-0.6}$
$norm_{compmag}$	$14.5^{+0.04}_{-0.05}$	22^{+8}_{-5}	16^{+10}_{-6}
E_{Fe} , keV	$6.4^{+0.1}_{-6.4}$	6.4 ± 0.1	6.50 ± 0.05
σ_{Fe} , keV	0.7 ± 0.1	$0.4^{+0.2}_{-0.1}$	$0.28^{+0.05}_{-0.06}$
$norm_{gauss}$, 10^{-4}	1.6 ± 0.2	1.9 ± 0.5	1.7 ± 0.2
C_{FPMB}	1.020 ± 0.004	1.023 ± 0.005	$1.022^{+0.002}_{-0.004}$
C_{XRT}	1.02 ± 0.02	1.09 ± 0.02	1.2 ± 0.2
$\chi^2_{reduced}/d.o.f.$	1.020/1694	0.995/1777	0.994/1463

¹The bolometric flux was calculated by the model from 0.02 keV to 50 keV, using $N_H = 0$.

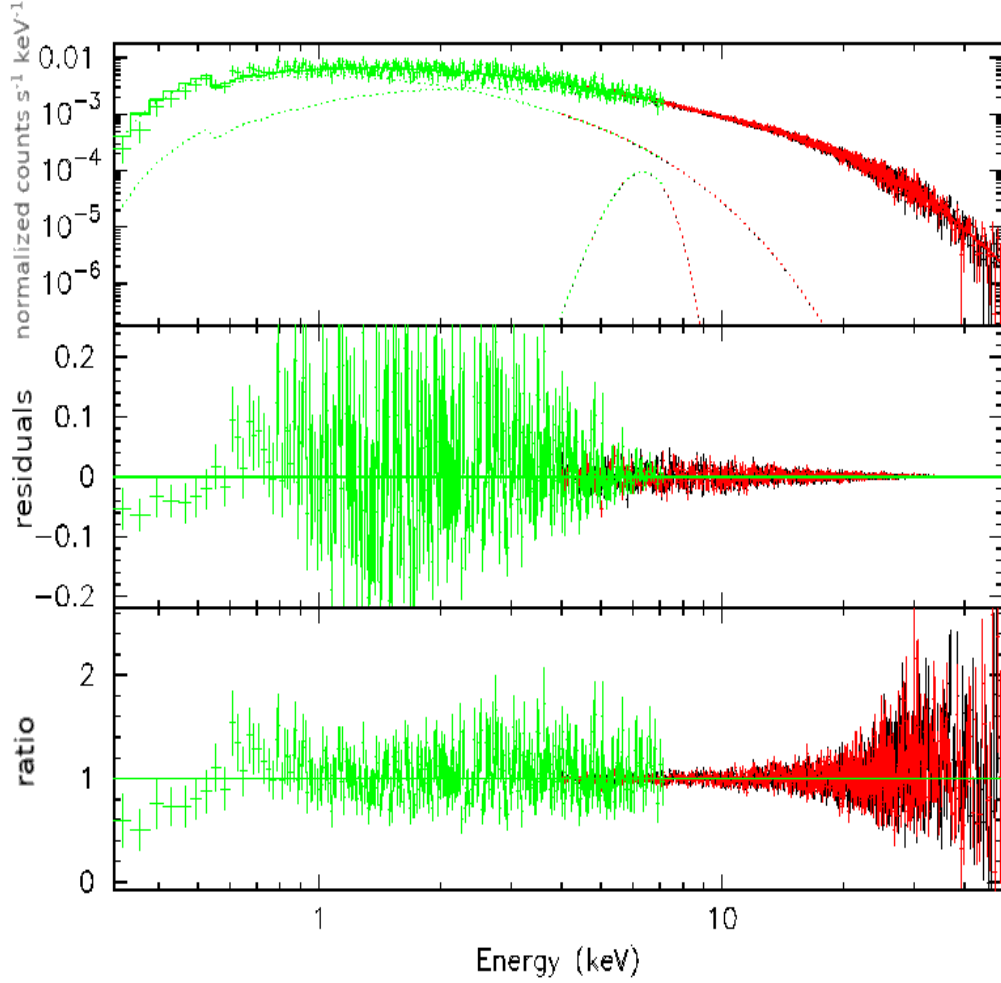


Figure 3.3: From top to bottom: (a) Energy spectrum of Observation 1 with the Model A best fit. We can differentiate the 3 modeling components of compmag, diskbb and gauss with the dotted lines. (b) Residuals of Model A best fit in normalized counts s⁻¹ keV⁻¹. (c) Ratio of Model A best fit. The green points show the Swift data and black and red points show the data from the FPMA and FPMB NuSTAR detectors respectively. The lines show the best fit models convolved with the instrument response.

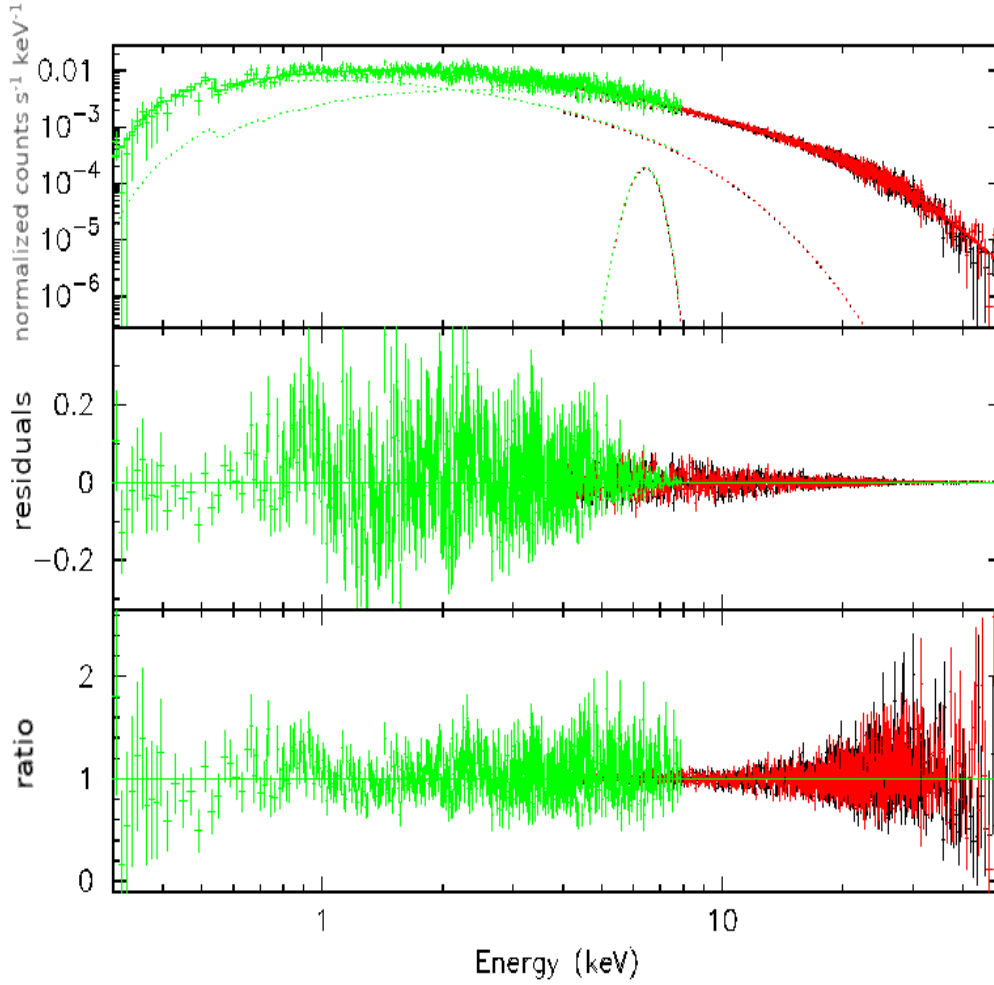


Figure 3.4: From top to bottom: (a) Energy spectrum of Observation 2 with the Model A best fit. We can differentiate the 3 modeling components of compmag, diskbb and gauss with the dotted lines. (b) Residuals of Model A best fit in normalized counts s⁻¹ keV⁻¹. (c) Ratio of Model A best fit. The green points show the Swift data and black and red points show the data from the FPMA and FPMB NuSTAR detectors respectively. The lines show the best fit models convolved with the instrument response.

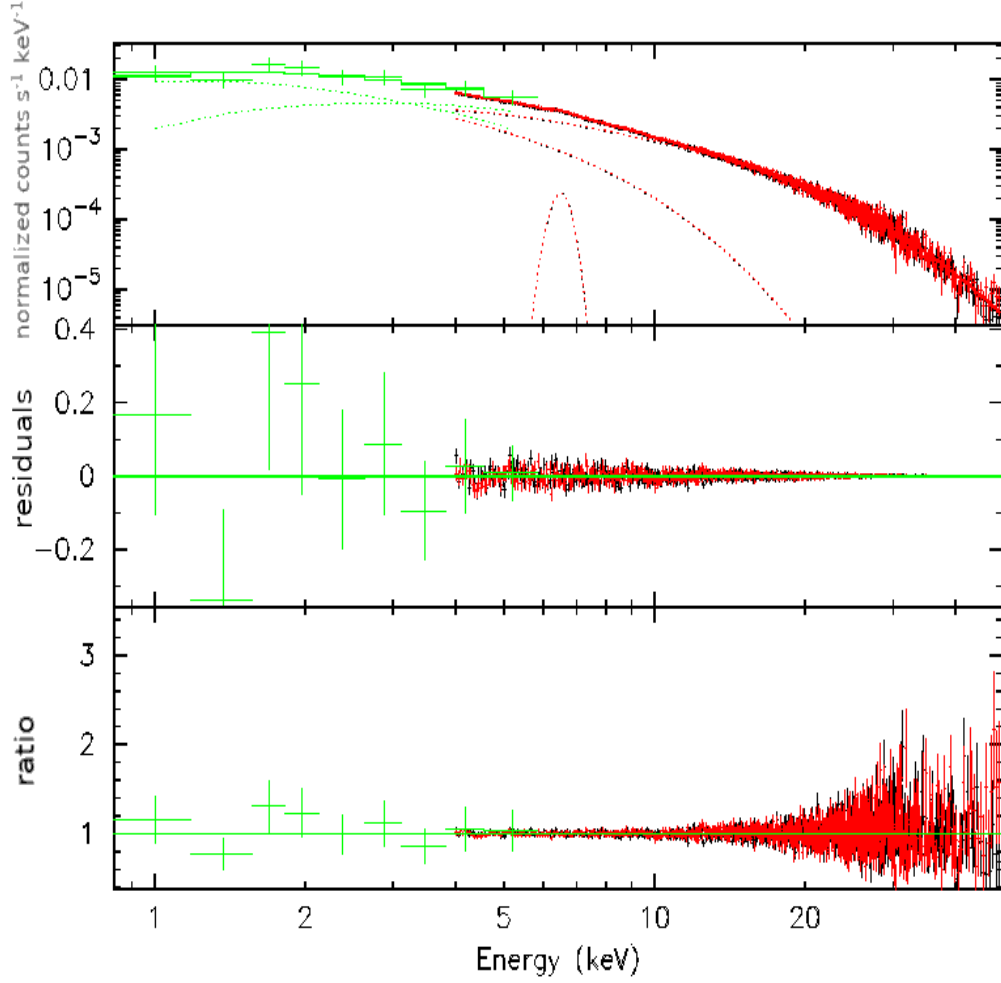


Figure 3.5: From top to bottom: (a) Energy spectrum of Observation 3 with the Model A best fit. We can differentiate the 3 modeling components of compmag, diskbb and gauss with the dotted lines. (b) Residuals of Model A best fit in normalized counts $\text{s}^{-1} \text{keV}^{-1}$. (c) Ratio of Model A best fit. Due to the low amount of photons in the WT mode of Swift, its data have an almost zero contribution to the modeling.

3.1.3 Model B Fitting

By examining the residuals and ratios of the *Model A* best fit, we can conclude that it is a good model for the data of all 3 observational instances. We could not distinguish any feature around 10 keV to 50 keV that resembled a cyclotron absorption line. Nevertheless, we tried fitting the data with *Model B*, but it did not yield any results. The search for a CRSF was, nonetheless, continued in our phase resolved analysis, because of the possibility of an absorption line being obscured by the phase averaged spectrum, but distinguishable in the phase resolved.

3.2 Pulse Profile of SXP 4.78

In this section we present the pulse profile of SXP 4.78 in different energy bands from both Swift and NuSTAR instruments. The energy bands for the Swift pulse profiles are [0.3 keV - 2 keV], where the accretion disk is more prominent and [2 keV - 8 keV]. The energy bands for the NuSTAR pulse profiles are [4 keV - 8 keV], [8 keV - 20 keV] and [20 keV - 50 keV].

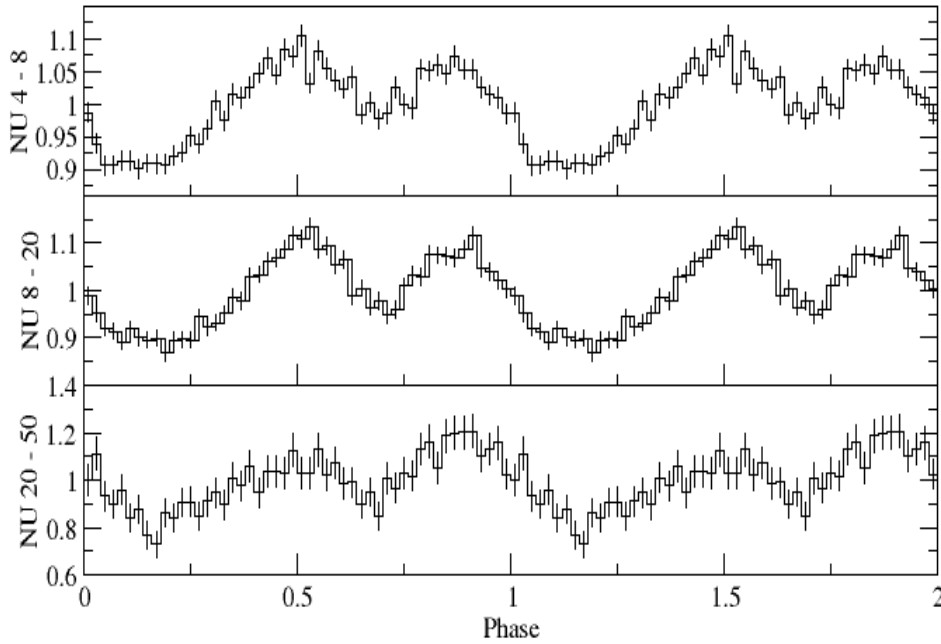


Figure 3.6: Pulse profile of Observation 3. The y-axis of every part is a normalized intensity series. The energy bands are from top to bottom: (a) NuSTAR from 4 keV to 8 keV. (b) NuSTAR from 8 keV to 20 keV. (c) NuSTAR from 20 keV to 50 keV.

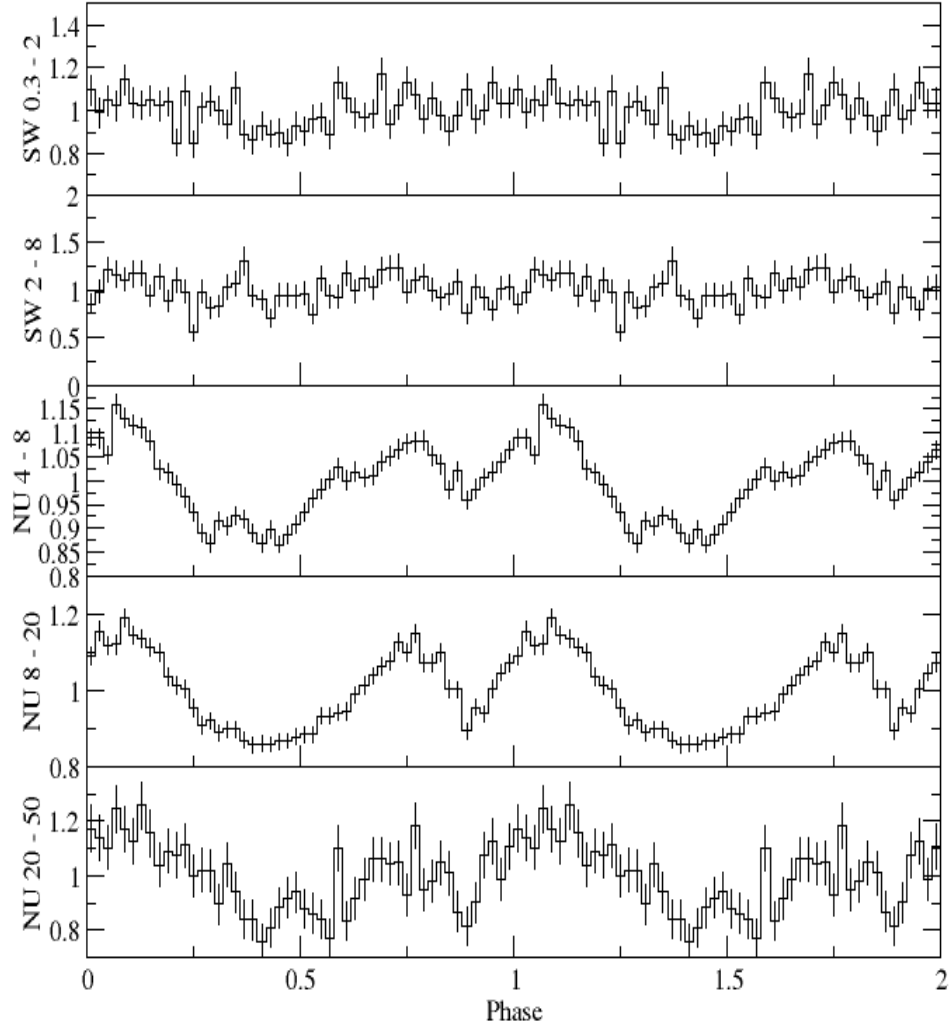


Figure 3.7: Pulse profile of Observation 2. The y-axis of every part is a normalized intensity series. The energy bands are from top to bottom: (a) Swift from 0.3 keV to 2 keV. (b) Swift from 2 keV to 8 keV. (c) NuSTAR from 4 keV to 8 keV. (d) NuSTAR from 8 keV to 20 keV. (e) NuSTAR from 20 keV to 50 keV.

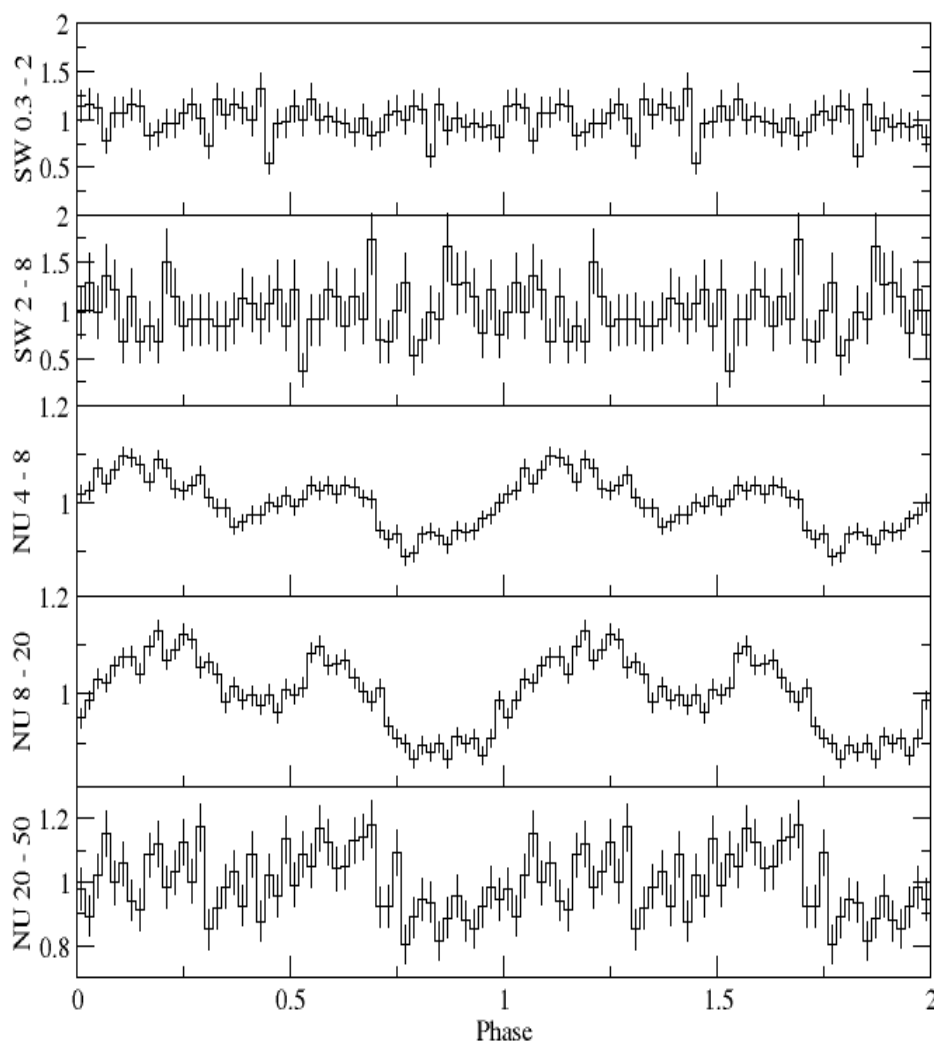


Figure 3.8: Pulse profile of Observation 1. The y-axis of every part is a normalized intensity series. The energy bands are from top to bottom: (a) Swift from 0.3 keV to 2 keV. (b) Swift from 2 keV to 8 keV. (c) NuSTAR from 4 keV to 8 keV. (d) NuSTAR from 8 keV to 20 keV. (e) NuSTAR from 20 keV to 50 keV.

3.3 Phase Resolved Analysis

Given that *Model A* was the simplest model that provided a good fit to the phase averaged spectra we adopted this model for the phase resolved spectra as well. This way we can study the evolution of the physical parameters of the accretion column depending on the pulse phase. After examining each parameter of the phase resolved results, we noticed that most of them remained constant within their uncertainty ranges, as it was expected. Those parameters were kT_{bb} , η , r_0 and the normalization factor of the compmag component, the T_{inn} and normalization factor of the diskbb component and the line energy and σ of the Gaussian component. The physical processes that each parameter describes explain the lack of their value fluctuation.

The blackbody component originates from the thermal mound above the magnetic pole of the pulsar, producing the seed photons that get up-scattered by the same interactions from the higher parts of the accretion column, regardless of the viewing angle we observe it, so it remains constant as a function of phase. The index of the velocity profile η is also non-dependent on the rotation, as it describes the general behaviour of the gas velocities. Due to the large error bars of the radius of the accretion column we conclude that r_0 is an unconstrained parameter. The Iron line energy and width (σ) are not dependent on the position of the accretion column, because the emission originates from the accretion disk. This is also true about the T_{inn} value of the diskbb component.

As a result, we decided to fit the remaining parameters while keeping frozen the other unconstrained ones to their phase averaged value. This was done to make the modeling process easier from a computational point of view. The behavior of the electron temperature, the vertical optical depth, the terminal velocity of the gas and the normalization factor of the Gaussian component are presented in the next section.

3.3.1 Observation 1

In Figure 3.9 we present the 4 fitted parameters of the Model A, as well as the change of flux, as a function of phase. The phase bins were grouped into 6 bins per 1 phase as showcased in the first panel of the figure with the black vertical lines.

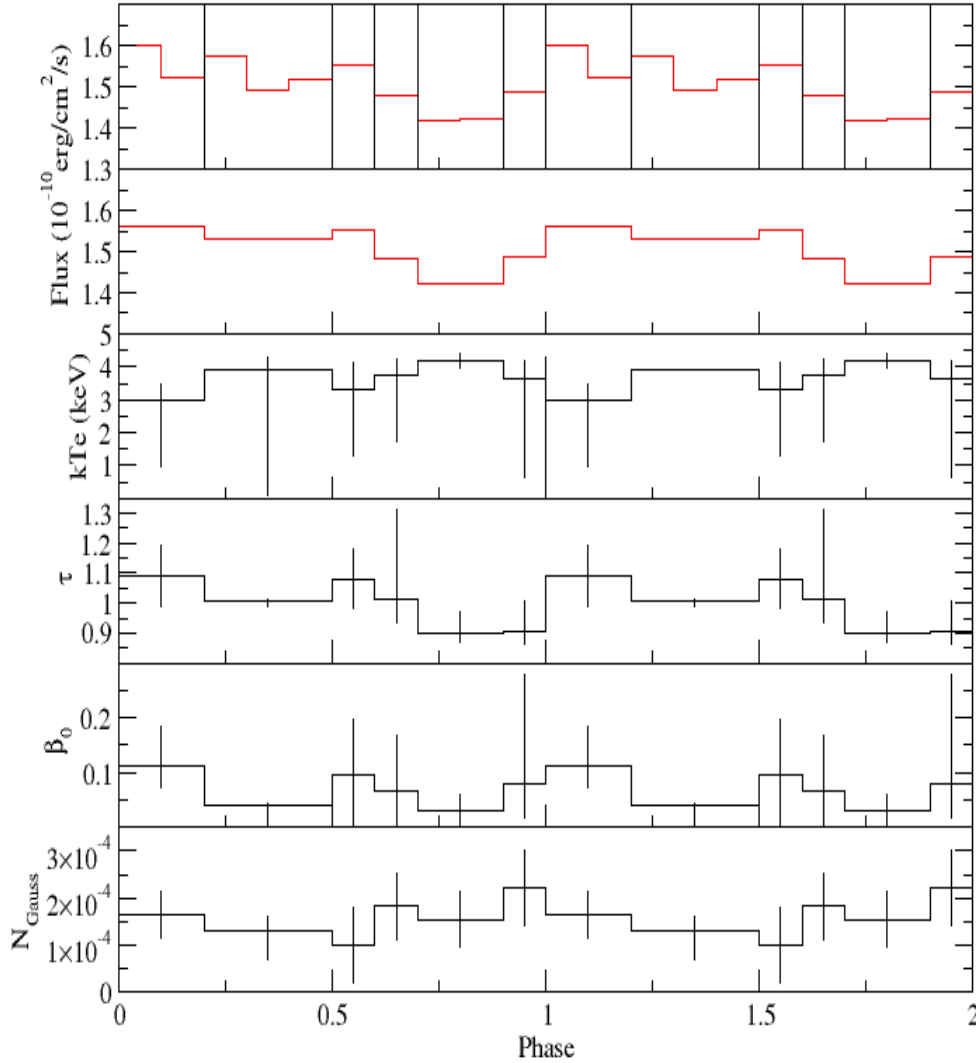


Figure 3.9: Phase resolved analysis results of the 4 variable parameters of Model A for Obs1. From top to bottom: (a) Flux (2 - 10 keV) as a function of phase for the initial bins and bin grouping selection. (b) Flux as a function of phase for the grouped bins. (c) Electron temperature as a function of phase. (d) Vertical optical depth as a function of phase in units of 10^{-3} of the Thomson cross section. (e) Electron terminal velocity as a function of phase in units of the speed of light. (f) Normalization factor of the Gaussian component as a function of phase.

3.3.2 Observation 2

In Figure 3.10 we present the 4 fitted parameters of the Model A, as well as the change of flux, as a function of phase. The phase bins were grouped into 6 bins per 1 phase as showcased in the first panel of the figure with the black vertical lines.

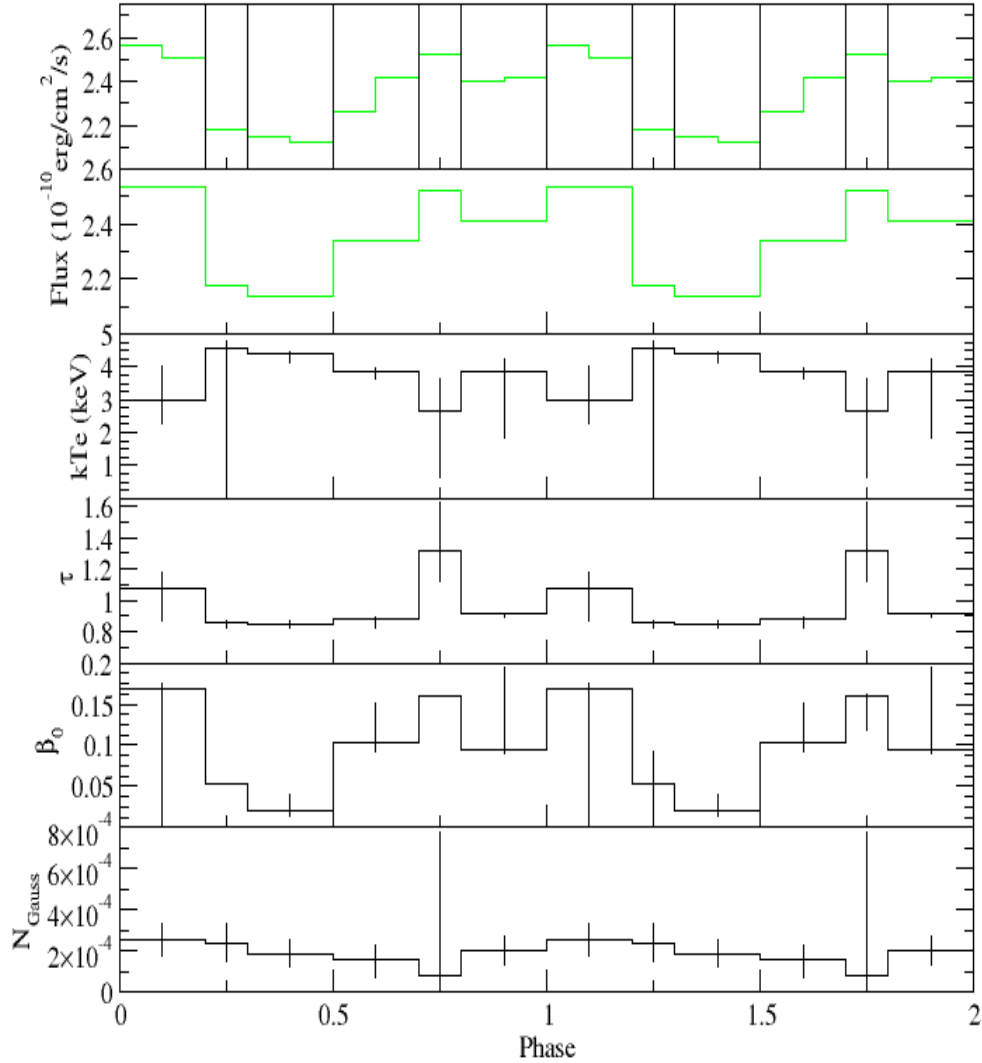


Figure 3.10: Phase resolved analysis results of the 4 variable parameters of Model A for Obs2. From top to bottom: (a) Flux (2 - 10 keV) as a function of phase for the initial bins and bin grouping selection. (b) Flux as a function of phase for the grouped bins. (c) Electron temperature as a function of phase. (d) Vertical optical depth as a function of phase in units of 10^{-3} of the Thomson cross section. (e) Electron terminal velocity as a function of phase in units of the speed of light. (f) Normalization factor of the Gaussian component as a function of phase.

3.3.3 Observation 3

In Figure 3.11 we present the 4 fitted parameters of the Model A, as well as the change of flux, as a function of phase. The phase bins were grouped into 8 bins per 1 phase. The black vertical lines showcase the grouping of the 2 pairs of bins.

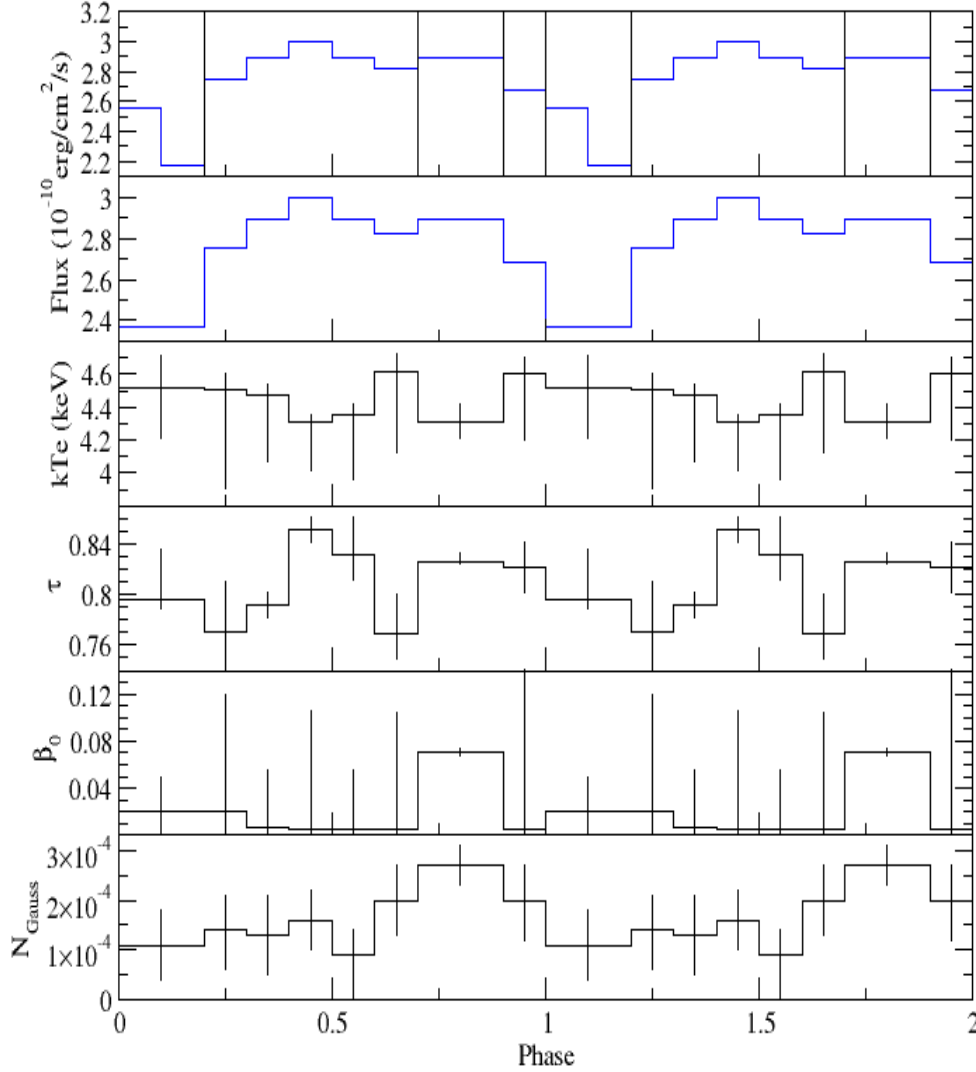


Figure 3.11: Phase resolved analysis results of the 4 variable parameters of Model A for Obs3. From top to bottom: (a) Flux (2 - 10 keV) as a function of phase for the initial bins and bin grouping selection. (b) Flux as a function of phase for the grouped bins. (c) Electron temperature as a function of phase. (d) Vertical optical depth as a function of phase in units of 10^{-3} of the Thomson cross section. (e) Electron terminal velocity as a function of phase in units of the speed of light. (f) Normalization factor of the Gaussian component as a function of phase.

3.3.4 Cyclotron Line Search

The ***Model B*** fit in the phase averaged data for all 3 observations did not produce any solid evidence of a CRSF. Regardless, one cannot exclude the possibility of a cyclotron absorption line being hidden in the phase averaged spectrum of a pulsar. The phase resolved analysis is capable of uncovering a CRSF in specific phases of a pulse, therefore we tried fitting Model B in the spectra of the bins of every observational instance.

However, in this case as well, ***Model B*** failed to distinguish any cyclotron absorption feature, in every phase of the 3 observations. We did not see any improvement in the residuals and the χ^2 of the phase resolved spectra fitted with Model B in comparison to Model A. The absence of a cyclotron absorption line comes in agreement with Semena et al. [2019](#).

Chapter 4

Discussion

4.1 Phase Averaged Analysis

The results of Table 3.2 can provide us with an estimate of the Eddington fraction (i.e. emitted luminosity over the Eddington luminosity) for each observation. The Eddington Luminosity is approximately (e.g. Bachetti et al. 2014):

$$L_{Edd.} \sim 2 \cdot 10^{38} \text{ erg/s} \quad (4.1)$$

After examining Table 3.2 we can conclude that during Obs1, the source remained at a sub-Eddington level, in contrast to the Obs2 and Obs3 where the pulsar emitted at super-Eddington rates.

In addition, the value of the blackbody parameter kT_{bb} is consistent with similar pulsar HMXBs, at approximately 1.2 keV - 1.3 keV (e.g. Tsygankov, Krivonos, and Lutovinov 2012; La Palombara et al. 2012). The vertical optical depth show a decreasing behavior (significant within the error bars) in between the 3 observations, from $\tau \sim 1$ in Obs1 to $\tau \sim 0.85$ in Obs3. That means that the light we observe during Obs1 originates from deeper inside the accretion column, while, as we move towards Obs3, we observe light from the outer parts of the column. The terminal velocity of the accreting matter can be considered constant within the errors.

4.1.1 Accretion Disk

The "diskbb" modeling component gave us great insight into the accretion disk. The T_{inn} values of Table 3.2 show an increase in the temperature of the inner radius of the accretion disk. The normalization factor provides us with an estimation of the inner radius of the disk. Using Eq.4.2 from the definition of the diskbb

component and Eq.2.3, we calculate the true inner radius (see Table 4.1).

$$r_{inn} = D_{10} \cdot \sqrt{\frac{norm}{\cos\theta}} \quad (4.2)$$

Table 4.1: Inner radius of the accretion disk of SXP 4.78.

Observation	norm _{diskbb}	True Inner Radius (km)
Obs1	0.57	9.0
Obs2	0.35	7.0
Obs3	0.48	8.2

The values of the inner radius in Table 4.1 suggest that the accretion disk is greatly evolved, reaching close to the surface of the neutron star. This is consistent with the existence of the Iron emission line. The photons that originate from the pulsar illuminate the disk, ionizing the Fe atoms that then emit light at approximately 6.4 keV.

4.1.2 Magnetic Field Strength

Even though we could not detect a cyclotron line which would give us a direct measurement of the magnetic field, we can use the bolometric luminosity to set an upper limit on the magnetic field strength. By applying Eq.4.3 (Tsygankov, Lutovinov, et al. 2016) we can calculate the upper boundary of the magnetic field in order to have accretion onto the compact object. The equation originates from the critical luminosity a source can emit, below which the magnetic field strength in combination with the rotation of the pulsar can expel matter away from the neutron star, in an effect known as "Propeller Effect" (Illarionov and Sunyaev 1975). Assuming the magnetospheric radius is smaller than the co-rotating radius, which corresponds to the radius where gas can be captured by the gravitational well of the pulsar, matter originating from the donor star can be accreted onto the compact object. By equating the co-rotating and the magnetospheric radius we can calculate the maximum allowed strength of the magnetic field in order for accretion to occur.

$$B_{12}^{max} \approx \frac{1}{2} \cdot 10^{37} L_{bol}^{1/2} P^{7/6} M_{1.4}^{1/3} R_6^{-5/2} k^{-7/4} \quad (4.3)$$

where B_{12}^{max} is the upper boundary of the magnetic field in units of $10^{12}G$, L_{bol} is the bolometric luminosity of the source in units of erg/s, P is the spin period of the pulsar, $M_{1.4}$ is its mass in units of $1.4 M_{\odot}$, R_6 is its radius in units of $10^6 cm$ and k is the ratio of the magnetospheric radius to the Alfvén radius, assuming spherical accretion. For a more detailed explanation of the accretion regimes see Stella, White, and Rosner 1986.

The values of L and P were acquired by Table 3.2 and Table 2.3 respectively. The radius of the pulsar was selected at $R_6 = 1.25$ (Suleimanov et al. 2016) and the value of k was set to 0.5 (Ghosh and Lamb 1978). The results of Eq.4.3 for all 3 observational instances are presented in Table 4.2. Since the magnetic field does not change, we can conclude that its maximum value is $B \sim 22.7 \cdot 10^{12} G$.

Table 4.2: Upper boundaries of the magnetic field of SXP 4.78.

Observation	L_{bol} (10^{38} erg/s)	B_{max} (10^{12} G)
Obs1	1.448	22.732
Obs2	2.138	27.628
Obs3	2.477	29.738

4.2 Pulse Profiles

The pulse profiles of SXP 4.78 in different energy bands uncover the behavior of soft and hard X-rays during a complete revolution of the pulsar. It is clear in all 3 observational instances that the pulse comprises of a pulse-on state with 2 peaks (see e.g. Figure 3.7 phase 0.1 and 0.75), originating from each of the magnetic poles of the pulsar, a small inter-pulse between the peaks and a pulse-off state with low flux (see e.g. Figure 3.7 phase 0.4 and 0.87).

During Obs1 and Obs2 (see Figures 3.8 and 3.7 respectively) we observe a lack of fluctuations in the Swift energy bands of 0.3 keV - 2 keV and 2 keV - 8 keV. The majority of those soft X-ray photons originate from the accretion disk. Since the spin of the pulsar does not greatly affect the accretion disk, we do not observe any changes, although, since there is a clear variation in the NU 4-8, we do expect a similar behaviour for SW 2-8. The large error bars of Swift and the less variable nature of the light below 4 keV mixing with the higher energies could explain the lack of variability in the 2-8 keV range of Swift.

As we move to harder X-rays, we can distinguish a steeper pulse, especially during Obs2 and Obs3 (see Figures 3.7 and 3.6 - NU 8-20). In addition, the inter-pulses during all 3 observational instances are more shallow in the NuSTAR 20 keV - 50 keV energy range. Therefore, we can conclude that the accretion column mainly emits in the range of 4 keV - 20 keV, where we observe the most variability.

4.3 Phase Resolved Analysis

An important aspect of the phase resolved analysis in this thesis is that we can only directly compare results between the different phases only within each observation. Comparison of the phase resolved results between observations require the registration of the phases between the different observations. This is a result of the

many days that passed between the observational instances and the way the phase binning was applied. Since there is not an absolute calibration between the phases of the different observations, we can only discuss the behaviour of parameters in their relative pulse-on and pulse-off parts of the pulse profile.

The electron temperature (kTe) appears to remain constant within its confidence range during Obs1, approximately around its phase averaged value of 3.6 keV (see Table 3.2). This is also true about Obs2 and Obs3. The vertical optical depth shows a small fluctuation following the flux of the pulsar in all 3 observational instances, especially in Obs2 and Obs3 (see Figures 3.10 and 3.11). The largest variation is observed during Obs3, with τ reaching 0.85 during pulse-on and dropping to 0.795 during pulse-off and 0.77 during the inter-pulse, a statistically significant change (see Figure 4.1). The terminal velocity of the gas also appears to follow the behavior of the flux during Obs2. The variation of β_0 covers the range from 0.03c during pulse-off to 0.16c during pulse-on. The large error bars of β_0 during Obs1 and Obs3 do not allow us to make any statements about changes in the electron terminal velocity. Finally, the normalization factor of the Gaussian line (i.e. its flux) appears to remain constant during Obs1 and Obs2, but a small, yet statistically significant fluctuation can be seen during Obs3 (see Figure 3.11), ranging from 10^{-4} during pulse-off and $2.8 \cdot 10^{-4}$ during pulse-on.

4.4 Time Evolution

The variations of τ , β_0 and the Gaussian normalization factor between pulse-on and pulse-off states of all 3 observational instances are presented in Figure 4.1. The data was acquired from the phase resolved analysis. As time passes and the pulsar becomes super-Eddington we can see that the optical depth is decreasing in both pulse-on and pulse-off, with a more significant change on the pulse-on state.

4.5 Further Work

The results presented in this thesis are considered promising. In order to fully understand the behavior of SXP 4.78 we can add previous and followup observations of the source, such as Chandra observations that took place on the 1st of March 2019 (ObsID. 22095). By studying an X-ray pulsar on the lowest observed intensity we can acquire a more strict constraint on the magnetic field intensity. Regarding the pulse profile, we can apply pulse profile models as a means to separate the fan beam and pencil beam radiation in the phase resolved analysis.

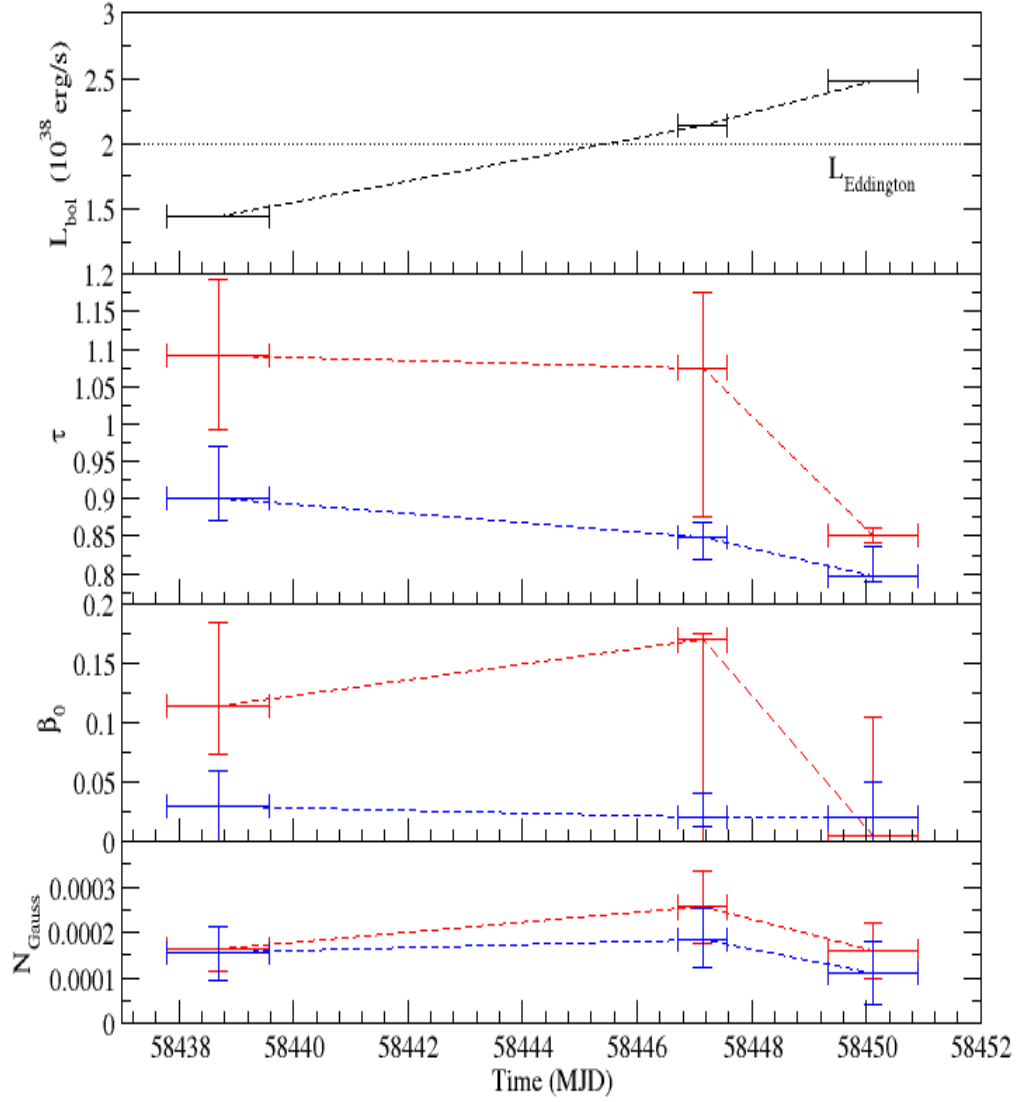


Figure 4.1: Time evolution of variable parameters during pulse-on (red) and pulse-off (blue). From top to bottom: (a) L_{bol} as a function of time. The Eddington luminosity is represented by the dotted line. (b) Vertical optical depth as a function of time in units of 10^{-3} of the Thomson cross section. (c) Electron terminal velocity as a function of time in units of the speed of light. (d) Normalization factor of the Gaussian component as a function of time.

Chapter 5

Conclusion

In this thesis, we have presented the spectral and timing analysis for the X-ray pulsar SXP 4.78. The pulsar is part of a Be/X-ray binary system in the SMC and it was observed in 3 instances by NuSTAR and Swift space telescopes. The observations took place from the 15th till the 28th of November of 2018 in the total energy range of 0.2 keV to 78.4 keV. By performing the data reduction, cleaning and calibration, we extracted the sky images, lightcurves and energy spectra of the source. The lightcurves were used to determine the pulsar's spin at 4.7816 ± 0.0002 and the spectra were analyzed using XSPEC.

We showed that a model composed of the compmag component of Becker and Wolff 2007 together with a disk blackbody, a Gaussian emission line and photoelectric absorptions give a very good fit, especially in Obs2 and Obs3, while simultaneously acquiring information about the physical conditions inside the accretion column. The diskbb component uncovered a fully developed accretion disk with its inner radius reaching the surface of the neutron star. An upper boundary for the magnetic field of the pulsar was also calculated, concluding that $B \lesssim 22.7 \cdot 10^{12} G$. In addition, we did not find significant variations of the physical parameters of the accretion column as a function of phase. Finally, we find no evidence for a cyclotron absorption line (CRSF) in either the phase averaged nor the phase resolved data.

References

- Bachetti, M. et al. (Oct. 2014). “An ultraluminous X-ray source powered by an accreting neutron star.” In: *Nature* 514.7521, pp. 202–204. DOI: [10.1038/nature13791](#). arXiv: [1410.3590 \[astro-ph.HE\]](#).
- Basko, M. M. and R. A. Sunyaev (May 1976). “The limiting luminosity of accreting neutron stars with magnetic fields.” In: *Monthly Notices of the Royal Astronomical Society* 175, pp. 395–417. DOI: [10.1093/mnras/175.2.395](#).
- Becker, D. Klochkov, et al. (Aug. 2012). “Spectral formation in accreting X-ray pulsars: bimodal variation of the cyclotron energy with luminosity.” In: *Astronomy and Astrophysics* 544, A123, A123. DOI: [10.1051/0004-6361/201219065](#). arXiv: [1205.5316 \[astro-ph.HE\]](#).
- Becker and Michael T. Wolff (2007). “Thermal and Bulk Comptonization in Accretion-powered X-Ray Pulsars.” In: *The Astrophysical Journal* 654.1, pp. 435–457. DOI: [10.1086/509108](#).
- Belenkaya, Elena S., Maxim L. Khodachenko, and Igor I. Alexeev (2015). “Alfvén Radius: A Key Parameter for Astrophysical Magnetospheres.” In: *Characterizing Stellar and Exoplanetary Environments*. Ed. by Helmut Lammer and Maxim Khodachenko. Cham: Springer International Publishing, pp. 239–249. ISBN: 978-3-319-09749-7. DOI: [10.1007/978-3-319-09749-7_12](#). URL: https://doi.org/10.1007/978-3-319-09749-7_12.
- Christodoulou, D. M., S. G. T. Laycock, and D. Kazanas (Sept. 2017). “Retrograde accretion discs in high-mass Be/X-ray binaries.” In: *Monthly Notices of the Royal Astronomical Society* 470.1, pp. L21–L24. DOI: [10.1093/mnrasl/slx058](#).
- Corbet, R., F. E. Marshall, and C. B. Markwardt (Jan. 2001). “XTE J0052-723.” In: *IAU Circulars* 7562, p. 1.
- Farinelli, R. et al. (Feb. 2012). “Numerical solution of the radiative transfer equation: X-ray spectral formation from cylindrical accretion onto a magnetized neutron star.” In: *Astronomy and Astrophysics* 538, A67, A67. DOI: [10.1051/0004-6361/201118008](#). arXiv: [1111.6851 \[astro-ph.HE\]](#).
- Finlay, C. C. et al. (2010). “International Geomagnetic Reference Field: the eleventh generation.” In: *Geophysical Journal International* 183.3, pp. 1216–1230. DOI: [10.1111/j.1365-246x.2010.04804.x](#).
- Galloway, D. K. et al. (July 2001). “Accretion column eclipses in the X-ray pulsars GX 1+4 and RX J0812.4-3114.” In: *Monthly Notices of the Royal Astronomical Society* 325.1, pp. 419–425. DOI: [10.1046/j.1365-8711.2001.04467.x](#). arXiv: [astro-ph/0010523 \[astro-ph\]](#).

- Gehrels, N. et al. (Aug. 2004). “The Swift Gamma-Ray Burst Mission.” In: *Astrophysical Journal* 611.2, pp. 1005–1020. DOI: [10.1086/422091](#). arXiv: [astro-ph/0405233](#) [[astro-ph](#)].
- Ghosh, P. and F. K. Lamb (July 1978). “Disk accretion by magnetic neutron stars.” In: *Astrophysical Journal, Letters* 223, pp. L83–L87. DOI: [10.1086/182734](#).
- Graczyk, Dariusz et al. (Nov. 2020). “A Distance Determination to the Small Magellanic Cloud with an Accuracy of Better than Two Percent Based on Late-type Eclipsing Binary Stars.” In: *Astrophysical Journal* 904.1, 13, p. 13. DOI: [10.3847/1538-4357/abbb2b](#). arXiv: [2010.08754](#) [[astro-ph.GA](#)].
- Harrison, Fiona A. et al. (June 2013). “The Nuclear Spectroscopic Telescope Array (NuSTAR) High-energy X-Ray Mission.” In: *Astrophysical Journal* 770.2, 103, p. 103. DOI: [10.1088/0004-637X/770/2/103](#). arXiv: [1301.7307](#) [[astro-ph.IM](#)].
- Illarionov, A. F. and R. A. Sunyaev (Feb. 1975). “Why the Number of Galactic X-ray Stars Is so Small?” In: *Astronomy and Astrophysics* 39, p. 185.
- Karino, Shigeyuki, Kenji Nakamura, and Ali Taani (June 2019). “Stellar wind accretion and accretion disk formation: Applications to neutron star high-mass X-ray binaries.” In: *Publications of the Astronomical Society of Japan* 71.3, 58, p. 58. DOI: [10.1093/pasj/psz034](#). arXiv: [1903.03455](#) [[astro-ph.HE](#)].
- Kirsch, Marcus G. F. et al. (Feb. 2004). “Timing accuracy and capabilities of XMM-Newton.” In: Society of Photo-Optical Instrumentation Engineers (SPIE) Conference Series 5165. Ed. by Kathryn A. Flanagan and Oswald H. W. Siegmund, pp. 85–95. DOI: [10.1117/12.503559](#).
- Kubota, Aya et al. (Dec. 1998). “Evidence for a Black Hole in the X-Ray Transient GRS 1009-45.” In: *Publications of the ASJ* 50, pp. 667–673. DOI: [10.1093/pasj/50.6.667](#).
- Kudritzki, Rolf-Peter and Joachim Puls (2000). “Winds from Hot Stars.” In: *Annual Review of Astronomy and Astrophysics* 38.1, pp. 613–666. DOI: [10.1146/annurev.astro.38.1.613](#).
- La Palombara, N. et al. (Mar. 2012). “XMM-Newton observation of the persistent Be/NS X-ray binary pulsar RX J0440.9+4431.” In: *Astronomy and Astrophysics* 539, A82, A82. DOI: [10.1051/0004-6361/201118221](#). arXiv: [1112.5341](#) [[astro-ph.HE](#)].
- Maravelias, G. et al. (Nov. 2018). “A B1-2e optical classification for the optical counterpart of XTE J0052-723 (SXP 4.78; Swift J005139.2-721704).” In: *The Astronomer’s Telegram* 12237, p. 1.
- Mitsuda, K. et al. (Jan. 1984). “Energy spectra of low-mass binary X-ray sources observed from Tenma.” In: *Publications of the ASJ* 36, pp. 741–759.
- Monageng, I. M. et al. (Oct. 2019). “An X-ray and optical study of the outbursting behaviour of the SMC Be X-ray binary SXP 91.1.” In: *Monthly Notices of the Royal Astronomical Society* 489.1, pp. 993–999. DOI: [10.1093/mnras/stz2262](#). arXiv: [1908.04638](#) [[astro-ph.HE](#)].
- Negueruela, I. et al. (Jan. 2006). “Supergiant Fast X-ray Transients: A New Class of High Mass X-ray Binaries Unveiled by INTEGRAL.” In: ESA Special Publication 604. Ed. by A. Wilson, p. 165. arXiv: [astro-ph/0511088](#) [[astro-ph](#)].
- Porter, John M. and Thomas Rivinius (Oct. 2003). “Classical Be Stars.” In: *Publications of the ASP* 115.812, pp. 1153–1170. DOI: [10.1086/378307](#).

- Reig, Pablo (2011). “Be/X-ray binaries.” In: *Astrophysics and Space Science* 332.1, pp. 1–29. DOI: [10.1007/s10509-010-0575-8](https://doi.org/10.1007/s10509-010-0575-8).
- Reisenegger, Andreas (July 2003). “Origin and evolution of neutron star magnetic fields.” In: *arXiv e-prints*, astro-ph/0307133, astro-ph/0307133. arXiv: [astro-ph/0307133](https://arxiv.org/abs/astro-ph/0307133) [astro-ph].
- Rezzolla, Luciano, Elias R. Most, and Lukas R. Weih (2018). “Using Gravitational-wave Observations and Quasi-universal Relations to Constrain the Maximum Mass of Neutron Stars.” In: *The Astrophysical Journal* 852.2, p. L25. DOI: [10.3847/2041-8213/aaa401](https://doi.org/10.3847/2041-8213/aaa401).
- Saxena, Sheetal (2020). “Multiwavelength Studies Of Gamma-Ray Emitting Radio Galaxies.” Doctoral Thesis. Universität Würzburg. DOI: [10.25972/OPUS-21538](https://doi.org/10.25972/OPUS-21538).
- Schönherr, G. et al. (2007). “A model for cyclotron resonance scattering features.” In: *Astronomy & Astrophysics* 472.2, pp. 353–365. DOI: [10.1051/0004-6361:20077218](https://doi.org/10.1051/0004-6361:20077218).
- Semena, Andrey N. et al. (Dec. 2019). “Observational constraints on the magnetic field of the bright transient Be/X-ray pulsar SXP 4.78.” In: *Monthly Notices of the Royal Astronomical Society* 490.3, pp. 3355–3364. DOI: [10.1093/mnras/stz2722](https://doi.org/10.1093/mnras/stz2722). arXiv: [1907.06241](https://arxiv.org/abs/1907.06241) [astro-ph.HE].
- Shimura, Toshiya and Fumio Takahara (June 1995). “On the Spectral Hardening Factor of the X-Ray Emission from Accretion Disks in Black Hole Candidates.” In: *Astrophysical Journal* 445, p. 780. DOI: [10.1086/175740](https://doi.org/10.1086/175740).
- Skelly, Clare (2022). *NASA Continues to Study Pulsars, 50 Years After Their Chance Discovery*. URL: <https://www.nasa.gov/feature/goddard/2017/nasa-continues-to-study-pulsars-50-years-after-their-chance-discovery>.
- Stella, L., N. E. White, and R. Rosner (Sept. 1986). “Intermittent Stellar Wind Acceleration and the Long-Term Activity of Population I Binary Systems Containing an X-Ray Pulsar.” In: *Astrophysical Journal* 308, p. 669. DOI: [10.1086/164538](https://doi.org/10.1086/164538).
- Suleimanov, Valery F. et al. (Dec. 2016). “The direct cooling tail method for X-ray burst analysis to constrain neutron star masses and radii.” In: *Monthly Notices of the Royal Astronomical Society* 466.1, pp. 906–913. ISSN: 0035-8711. DOI: [10.1093/mnras/stw3132](https://doi.org/10.1093/mnras/stw3132). eprint: <https://academic.oup.com/mnras/article-pdf/466/1/906/10865744/stw3132.pdf>. URL: <https://doi.org/10.1093/mnras/stw3132>.
- Tauris, T. M. and E. P. J. van den Heuvel (2006). “Formation and evolution of compact stellar X-ray sources.” In: 39, pp. 623–665.
- Tsygankov, S. S., R. A. Krivonos, and A. A. Lutovinov (Apr. 2012). “Broad-band observations of the Be/X-ray binary pulsar RX J0440.9+4431: discovery of a cyclotron absorption line.” In: *Monthly Notices of the Royal Astronomical Society* 421.3, pp. 2407–2413. DOI: [10.1111/j.1365-2966.2012.20475.x](https://doi.org/10.1111/j.1365-2966.2012.20475.x). arXiv: [1201.0616](https://arxiv.org/abs/1201.0616) [astro-ph.HE].
- Tsygankov, S. S. and A. A. Lutovinov (Feb. 2005). “Observations of the Transient X-ray Pulsar KS 1947+300 by the INTEGRAL and RXTE Observatories.” In: *Astronomy Letters* 31.2, pp. 88–97. DOI: [10.1134/1.1862348](https://doi.org/10.1134/1.1862348). arXiv: [astro-ph/0501080](https://arxiv.org/abs/astro-ph/0501080) [astro-ph].

- Tsygankov, S. S., A. A. Lutovinov, et al. (Aug. 2016). “Propeller effect in two brightest transient X-ray pulsars: 4U 0115+63 and V 0332+53.” In: *Astronomy and Astrophysics* 593, A16, A16. DOI: [10.1051/0004-6361/201628236](https://doi.org/10.1051/0004-6361/201628236). arXiv: [1602.03177](https://arxiv.org/abs/1602.03177) [[astro-ph.HE](#)].
- Wilms, J., A. Allen, and R. McCray (Oct. 2000). “On the Absorption of X-Rays in the Interstellar Medium.” In: *Astrophysical Journal* 542.2, pp. 914–924. DOI: [10.1086/317016](https://doi.org/10.1086/317016). arXiv: [astro-ph/0008425](https://arxiv.org/abs/astro-ph/0008425) [[astro-ph](#)].

DECLARATION

I certify that

- a. the work contained in the thesis is original and has been done by myself under the general supervision of my supervisor.
- b. the work has not been submitted to any other institute for any degree or diploma.
- c. I have followed the guidelines provided by the institute in writing the thesis.
- d. I have conformed to the norms and guidelines given in the ethical code of conduct of the institute.
- e. whenever I have used materials (data, theoretical analysis, and text) from other sources, I have given due credit to them by citing them in the text of the thesis and giving their details in the references.
- f. whenever I have quoted written materials from other sources, I have put them under quotation marks and given due credit to the sources by citing them and giving required details in the references.

Konstantinos Droudakis
30/09/2022

